

**ANL-76-79**

**ANL-76-79**

PLEASE RETURN TO  
MFC BRANCH LIBRARY

INL Technical Library



108379

**FUEL DYNAMICS LOSS-OF-FLOW TEST L3  
(FINAL REPORT)**

**Compiled by**

**A. K. Fischer, R. K. Lo,  
and E. W. Barts**

**BASE TECHNOLOGY**



U of C - AUA - USERDA

---

**ARGONNE NATIONAL LABORATORY, ARGONNE, ILLINOIS**

**Prepared for the U. S. ENERGY RESEARCH  
AND DEVELOPMENT ADMINISTRATION  
under Contract W-31-109-Eng-38**

The facilities of Argonne National Laboratory are owned by the United States Government. Under the terms of a contract (W-31-109-Eng-38) between the U. S. Energy Research and Development Administration, Argonne Universities Association and The University of Chicago, the University employs the staff and operates the Laboratory in accordance with policies and programs formulated, approved and reviewed by the Association.

#### MEMBERS OF ARGONNE UNIVERSITIES ASSOCIATION

The University of Arizona  
Carnegie-Mellon University  
Case Western Reserve University  
The University of Chicago  
University of Cincinnati  
Illinois Institute of Technology  
University of Illinois  
Indiana University  
Iowa State University  
The University of Iowa

Kansas State University  
The University of Kansas  
Loyola University  
Marquette University  
Michigan State University  
The University of Michigan  
University of Minnesota  
University of Missouri  
Northwestern University  
University of Notre Dame

The Ohio State University  
Ohio University  
The Pennsylvania State University  
Purdue University  
Saint Louis University  
Southern Illinois University  
The University of Texas at Austin  
Washington University  
Wayne State University  
The University of Wisconsin

#### NOTICE

This report was prepared as an account of work sponsored by the United States Government. Neither the United States nor the United States Energy Research and Development Administration, nor any of their employees, nor any of their contractors, subcontractors, or their employees, makes any warranty, express or implied, or assumes any legal liability or responsibility for the accuracy, completeness or usefulness of any information, apparatus, product or process disclosed, or represents that its use would not infringe privately-owned rights. Mention of commercial products, their manufacturers, or their suppliers in this publication does not imply or connote approval or disapproval of the product by Argonne National Laboratory or the U. S. Energy Research and Development Administration.

Printed in the United States of America  
Available from

National Technical Information Service  
U. S. Department of Commerce  
5285 Port Royal Road  
Springfield, Virginia 22161

Price: Printed Copy \$5.00; Microfiche \$3.00

---

ANL-76-79

---

ARGONNE NATIONAL LABORATORY  
9700 South Cass Avenue  
Argonne, Illinois 60439

FUEL DYNAMICS LOSS-OF-FLOW TEST L3  
(FINAL REPORT)

Compiled by

A. K. Fischer,\* R. K. Lo,  
and E. W. Barts\*\*

Major Contributors

L. W. Deitrich  
A. De Volpi  
C. C. Meek  
W. F. Murphy†  
G. S. Stanford

Reactor Analysis and Safety Division

June 1976

\*Chemical Engineering Division, ANL

\*\*Now at Los Alamos Scientific Laboratory, Los Alamos, N. M.

†Materials Science Division, ANL





## TABLE OF CONTENTS

	<u>Page</u>
ABSTRACT . . . . .	11
I. INTRODUCTION . . . . .	11
II. DESCRIPTION OF L3 TEST COMPONENTS . . . . .	13
A. TREAT Reactor . . . . .	13
B. Loop and Test Section . . . . .	13
C. Fuel Pins . . . . .	16
D. Instrumentation . . . . .	18
1. Thermocouples . . . . .	18
2. Flowmeters . . . . .	19
3. Pressure Transducers . . . . .	20
4. Hodoscope . . . . .	20
III. TEST L3, RUN 1 . . . . .	21
A. General Description and Data Graphs of Run 1 . . . . .	21
B. Calibration Factor for Test L3 . . . . .	24
C. Noteworthy Features of Run 1 . . . . .	24
IV. TEST L3, RUN 2 . . . . .	25
A. Power, Pressure, Flow, and Temperature Data . . . . .	25
B. Neutron Radiographs . . . . .	31
C. Hodoscope Results . . . . .	33
D. Results of Posttest Examination . . . . .	43
1. Disassembly of the Loop . . . . .	43
2. General Observations . . . . .	49
3. Fuel-column Region . . . . .	50
4. Extent of Melting . . . . .	53
5. Evidence for Flows of Molten Stainless Steel . . . . .	54
6. Morphology of the Fuel . . . . .	54
7. Plenum Region of Fuel Elements . . . . .	59
8. Powders . . . . .	62
9. Microprobe Examination of Samples . . . . .	66

## TABLE OF CONTENTS

	<u>Page</u>
V. DISCUSSION AND ANALYSIS OF TEST L3, RUN 2. . . . .	74
A. Scenario Constructed from Examination and Correlation of Experimental Data . . . . .	74
B. Rationale behind Scenario Deduction . . . . .	77
C. Commentary on the Scenario . . . . .	80
1. Comments on Instrumental Data, Excluding Hodoscope . . . .	80
2. Comments on Hodoscope Data . . . . .	83
3. Interpretation and Correlation of Results of Posttest Examination . . . . .	85
4. SAS2B Calculations . . . . .	87
APPENDIX: Test-section Characteristics . . . . .	88
ACKNOWLEDGMENTS . . . . .	90

## LIST OF FIGURES

<u>No.</u>	<u>Title</u>	<u>Page</u>
1.	Cutaway View of TREAT Facility . . . . .	14
2.	TREAT Core-loading Diagram for Test L3. . . . .	15
3.	General View of Test Section and Mark-IIA Loop. . . . .	15
4.	Details of PNL-17 Fuel Pin . . . . .	16
5.	Cross-sectional View of Arrangement of Fuel Pins and Instrumentation . . . . .	17
6.	Axial Positions of Thermocouples Relative to Fuel Pins . . . . .	18
7.	Test L3, Run 1: Reactor Power . . . . .	21
8.	Test L3, Run 1: Integrated Reactor Power. . . . .	21
9.	Test L3, Run 1: Inlet and Outlet Flowmeters . . . . .	22
10.	Test L3, Run 1: Inlet and Outlet Coolant Pressure . . . . .	22
11.	Test L3, Run 1: Inlet and Outlet Coolant Temperature . . . . .	22
12.	Test L3, Run 1: TC7 and TC8 Structure Temperature . . . . .	23
13.	Test L3, Run 1: TC9 and TC10 Structure Temperature . . . . .	23
14.	Test L3, Run 1: TC11 and TC12 Structure Temperature. . . . .	23
15.	Test L3, Run 1: TC13 and TC14 Structure Temperature. . . . .	24
16.	Test L3, Run 2: Reactor Power . . . . .	25
17.	Test L3, Run 2: Inlet Flow Rate. . . . .	25
18.	Test L3, Run 2: Outlet Flow Rate. . . . .	25
19.	Test L3, Run 2: Integrated Reactor Power. . . . .	26
20.	Test L3, Run 2: Inlet Flow Rate; Expanded Scale 29.7-30.5 s . . .	26
21.	Test L3, Run 2: Outlet Flow Rate; Expanded Scale 29.7-30.5 s . .	26
22.	Test L3, Run 2: Inlet Pressure . . . . .	27
23.	Test L3, Run 2: Outlet Pressure . . . . .	27
24.	Test L3, Run 2: Inlet Pressure; Expanded Scale 29.7-30.5 s . . .	27
25.	Test L3, Run 2: Outlet Pressure; Expanded Scale 29.7-30.5 s . . .	28
26.	Test L3, Run 2: TC1 Inlet Temperature . . . . .	28
27.	Test L3, Run 2: TC4 Outlet Temperature . . . . .	28
28.	Test L3, Run 2: TC5 Outlet Temperature . . . . .	28

## LIST OF FIGURES

<u>No.</u>	<u>Title</u>	<u>Page</u>
29.	Test L3, Run 2: TC7 Structure Temperature . . . . .	29
30.	Test L3, Run 2: TC8 Structure Temperature . . . . .	29
31.	Test L3, Run 2: TC9 Structure Temperature . . . . .	29
32.	Test L3, Run 2: TC10 Structure Temperature . . . . .	30
33.	Test L3, Run 2: TC11 Structure Temperature . . . . .	30
34.	Test L3, Run 2: TC12 Structure Temperature . . . . .	30
35.	Posttest Neutron Radiograph of Test L3. . . . .	32
36.	Hodoscope Channels in Relation to Test Section. . . . .	33
37.	Test L3 Fuel Configuration at 11 s with Respect to 8-s Configuration. . . . .	34
38.	Test L3 Fuel Configuration at 15 s with Respect to 8-s Configuration. . . . .	35
39.	Test L3 Fuel Configuration at 17.5 s with Respect to 8-s Configuration. . . . .	35
40.	Test L3 Fuel Configuration at 19 s with Respect to 8-s Configuration. . . . .	36
41.	Test L3 Fuel Configuration at 20.5 s with Respect to 8-s Configuration. . . . .	36
42.	Test L3 Fuel Configuration at 22 s with Respect to 8-s Configuration. . . . .	37
43.	Change in Test L3 Fuel Configuration between 20.5 and 22.0 s . . .	37
44.	Test L3 Fuel Configuration at 23.5 s with Respect to 8-s Configuration. . . . .	38
45.	Test L3 Fuel Configuration at 26 s with Respect to 8-s Configuration. . . . .	39
46.	Change in Test L3 Fuel Configuration between 22.0 and 26.0 s . . .	39
47.	Test L3 Fuel Configuration at 29.3 s with Respect to 8-s Configuration. . . . .	39
48.	Change in Test L3 Fuel Configuration due to Eructation between 29.72 and 29.98 s . . . . .	40
49.	Initial Fuel Motion Associated with Eructation at 29.77 s . . . . .	41
50.	Test L3 Fuel Configuration at 30.5 s with Respect to 8-s Configuration. . . . .	41

## LIST OF FIGURES

<u>No.</u>	<u>Title</u>	<u>Page</u>
51.	Change in Test L3 Fuel Configuration between End of Eructation and Scram; Time Interval: 31.2-33.9 s . . . . .	42
52.	Test L3 Fuel Configuration Just before Scram with Respect to 8-s Configuration. . . . .	42
53.	Sectioning Scheme for Test Section of Test L3 . . . . .	43
54.	Mirror Image of Left Half of Section 118A3; Fuel-containing Sections with Sodium . . . . .	44
55.	Mirror Image of Right Half of Section 118A3; Fuel-containing Sections with Sodium . . . . .	45
56.	Samples Initially Cut from Fuel-containing Part at Test Section. .	46
57.	Mirror Images of Sections 118A3L and 118A13L after Sodium Removal, Showing Blockages at Bottom of Elements at Lower Right and above Fuel Mass at Upper Left. . . . .	46
58.	Mirror Images of Sections 118A12R and 118A15R after Sodium Removal, Showing Melting of Element 17-15 above Fuel Column and Meltthrough of Outer Test-section Tube. . . . .	47
59.	Mirror Images of Section 118A17R after Sodium Removal, Showing Front and Back Views of Bellows and Inside of Loop Wall at Midlength of Original Fuel Region . . . . .	47
60.	Mirror Image of Section 118A19R after Sodium Removal, Showing Bottom Blockage and Backside of Test-section Tube after Separation from Loop Wall. . . . .	48
61.	Mirror Image of Bottom End Plug after Sodium Removal . . . . .	48
62.	Mirror Images of Transverse Sections from Vicinity of Bottom Blockage below Header. . . . .	50
63.	Composite of Transverse Sections through Bottom Blockage, Showing Distribution of Fuel and Melted Stainless Steel . . . . .	51
64.	Bottom of Fuel Column, Showing Stainless Steel Blockage; Section 118A19R . . . . .	51
65.	Mirror Images of Transverse Sections at Upper Blockage, Showing Relationship of Pellets and Melted Stainless Steel . . . . .	52
66.	Composite of Transverse Section at Upper Blockage, Showing Partial Melting of Outer Test-section Tube . . . . .	52
67.	Transverse Section through Top of Bottom End Plugs, Showing Two Types of Melted Material . . . . .	55

## LIST OF FIGURES

<u>No.</u>	<u>Title</u>	<u>Page</u>
68.	Cast Steel Structure at Two Locations Next to Bottom End Plugs .	55
69.	Dispersion of Stainless Steel Globules in Melted Fuel. . . . .	56
70.	Melted Fuel with No Metallic Particles from Approximate Midlength of Original Fuel Column . . . . .	57
71.	Intrusion of Metal into Unmelted Fuel at Top of Fuel Column. . .	57
72.	Cracked, Unmelted Fuel from Bottom Pellet. . . . .	58
73.	Grain-size Variation in Upper Fuel Mass. . . . .	58
74.	Porosity within Grains of Melted Fuel at Top of Upper Mass of Fuel. . . . .	58
75.	Composite of Transverse Section near Original Midplane of Fuel Column with Large Frothlike Bubble of Fuel. . . . .	59
76.	Fuel Deposited on a Thermocouple between Outer Tube and Inner Fluted Tube . . . . .	60
77.	Metallic Ingot Recovered from Spacer Tube; Section 118A4. . . .	60
78.	Relative Pre- and Posttest Locations of Spring and Spacer in Plenums of Fuel Pins . . . . .	61
79.	Particulate Material from Fuel Sections of Loop. . . . .	63
80.	Powder Sample from Lower Bend of Loop . . . . .	63
81.	Cumulative Size Distribution of Particles. . . . .	65
82.	Section 118A46 through Top of Bottom End Plugs, Showing Composition of Metal and Fuel. . . . .	67
83.	Section 118A30R2, Showing Locations of Microprobe Analysis . . .	68
84.	Section 118A23L2, Showing Locations of Microprobe Analysis . . .	71
85.	Sample Current and Elemental Distribution Images of Two Types of Steel Particles from Section 118A23L2 . . . . .	72
86.	Scenario from Test L3, Run 2 . . . . .	74
87.	Vapor Pressures of Fuel and Stainless Steel. . . . .	83
A.1.	Loop for Test L3. . . . .	89

## LIST OF TABLES

<u>No.</u>	<u>Title</u>	<u>Page</u>
I.	PNL-17 Fuel-pin Characteristics . . . . .	17
II.	Test L3, Run 2: Experimental Parameters. . . . .	31
III.	Weights and Densities of Powders Recovered from Test L3. . . . .	64
IV.	Distribution of Powders along Length of Test Section . . . . .	64
V.	Particle-size Distribution in Powders Recovered from Sections 3L and 17R . . . . .	65
VI.	Composition of Stainless Steel in Section 118A46 . . . . .	67
VII.	Composition of Stainless Steel, Nickel Braze, and Metal Particles in Fuel of Section 118A30R2 . . . . .	69
VIII.	Instrumental Responses to Events in Test L3, Run 2. . . . .	75
IX.	Fuel Deficit below Row 12 . . . . .	84
X.	Scenario Derived from SAS Calculations. . . . .	87
A.1.	Axial Parameters of Fuel Pin and Cross Section of Test L3. . . . .	88





## FUEL DYNAMICS LOSS-OF-FLOW TEST L3 (FINAL REPORT)

Compiled by

A. K. Fischer, R. K. Lo,  
and E. W. Barts

### ABSTRACT

The behavior of FTR-type, mixed-oxide, preirradiated, "intermediate-power-structure" fuel during a simulation of an FTR loss-of-flow accident was studied in the Mark-IIA integral TREAT loop. Analysis of the data reported here leads to a postulated scenario (sequence and timing) of events in the test. This scenario is presented, together with the calculated timing of events obtained by use of the SAS code.

The initial fuel motion, starting during the preheat phase, consisted of coherent motion of the entire intact fuel bundle toward the pump. Incoherence developed as temperature rose. The fuel motion was mostly upward, and the greatest was in the top third of the fuel column. Fuel fragments formed against the pump side of the fluted tube near the original fuel midplane. A penetration of fluted tube occurred. A sudden voiding of the central region of the fuel column occurred at 29.75 s and was largely completed within 150 ms.

The lower steel blockage of the fuel elements occurred in the vicinity of the lower insulator pellets. The upper steel blockage just above the tops of the original fuel pins appeared to have channels through it. Cladding and spacer wires melted away in the fuel section. Fuel pellets were only evident at and above the top and at the bottom of the original fuel column, where a large mass of melted fuel was present. Over the length of the fuel column, most of the fluted tube had melted away.

### I. INTRODUCTION

The objective of the Fuel Dynamics L-series tests is to provide direct and interpreted experimental information bearing on the behavior of LMFBR fuel elements under conditions of loss of flow of coolant. This information supports the RAS Accident Analysis Group in its efforts to provide an analytical description of an FTR unprotected Flow Coastdown Accident. The experiments, done in the Transient Reactor Test Facility (TREAT), embody

approximations of the sequence of flow-coastdown accidents insofar as the events in the sequence can be simulated within the constraints of the available facilities. Identified events in the sequence are flow coastdown, heating of the fuel and cladding, gas release from the pin plenums, coolant boiling and voiding of the heated zone, cladding dryout, cladding melting and relocation, fuel melting, and possible fuel slumping, frothing, or other fuel-motion effects. Reactivity changes as consequences of fuel motion were not included in the execution of recent L-series tests.

Four L-series tests have been performed. An exploratory experiment, L1\*, which did not produce pin failure was done with a single fresh fuel pin. Test L2\*\* was the first in which loss of flow caused fuel-pin destruction. Tests L2, L3, and L4\*\* involved clusters of seven pins containing, respectively, fresh fuel, low-power (no central void) irradiated fuel, and high-power (fully developed central void) irradiated fuel. This series therefore provides an experimental comparison between fresh fuel and irradiated fuel under loss-of-flow (LOF) conditions. Gross features of the experiments were similar, but there were some differences, besides degree of burnup, such as specific types of pins and TREAT power levels. Minor variations also occurred in initial coolant temperature and duration of flow coastdown.

---

\*J. C. Cutter, R. T. Purviance, J. F. Boland, and C. E. Dickerman, First Loss of Flow Experiment with an FTR-Type Fuel Pin in the Mark-II Loop, Nucl. Technol. 14, 133 (May 1972).

\*\*E. W. Barts, L. W. Dietrich, J. G. Eberhart, A. K. Fisher, and C. C. Meek, Summary and Evaluation—Fuel Dynamics Loss-of-Flow Experiments (Tests L2, L3 and L4), ANL-75-57, September 1975.

## II. DESCRIPTION OF L3 TEST COMPONENTS

### A. TREAT Reactor

Irradiations for the L-series tests were done at the Idaho National Engineering Laboratory in the TREAT reactor. TREAT has the ability to maintain a constant power level in the test pins for up to about 30 s. A cut-away view of the TREAT facility is shown in Fig. 1. The maximum thermal-neutron flux, about  $9 \times 10^{15}$  n/cm<sup>2</sup>-s, provides an adequate means of inducing the heat effects to be studied in safety research experiments relating to fast reactors. The maximum temperature allowed during these experiments for the TREAT core is 1112°F (600°C). Core elements in TREAT have a 4-in.-sq cross section. Two such elements were removed from the center of the core to provide space for insertion of the test vehicle, the Mark-II loop. Figure 2 shows the TREAT loading diagram for Test L3. The fuel region of the test section in this loop was monitored by the fast-neutron hodoscope.

For L3, the reactor power was controlled in order to provide an initial 2-s surge that was about 67% higher than the following steady power level. This steady power was maintained until the programmed scram was executed. The early surge allowed the steady-state conditions to be established sooner than in the absence of the surge and thus allowed more time for the development of postcoastdown events.

### B. Loop and Test Section

A general view of the L3 test section and the Mark-IIA loop is shown in Fig. 3. The Mark-IIA loop is a self-contained unit that occupies the place of two adjacent core elements (a 4 x 8-in. space) in TREAT. An annular linear-induction pump (ALIP) drives sodium in a clockwise circuit, as seen in Fig. 3, so that the flow is upward in the test section. Sodium can move upward into the region of the test-section extension, either from thermal expansion or from pressure pulses that arise during an experiment. A safety pressure relief is available to dump the coolant into a dump tank if dangerously high pressures develop.

The coolant flow coastdown in Test L3-2, achieved by cutting back power to the loop pump, reduced the sodium flow rate to about 10% of its initial value within about 4-5 s. A table and a diagram giving details relevant to loop hydraulics are shown in the appendix.

Except for some details, the L3 test section was like the one in L2. The outer-shell thickness of the test section was 0.030 in., except for the bellows, where it was 0.006 in. (L2 had a thinner shell). Unlike L2, no void detector was used in L3. A dysprosium shaping collar with two zones of different thicknesses was used, as in L2, at each end of the test section to minimize power peaking at the fuel ends.

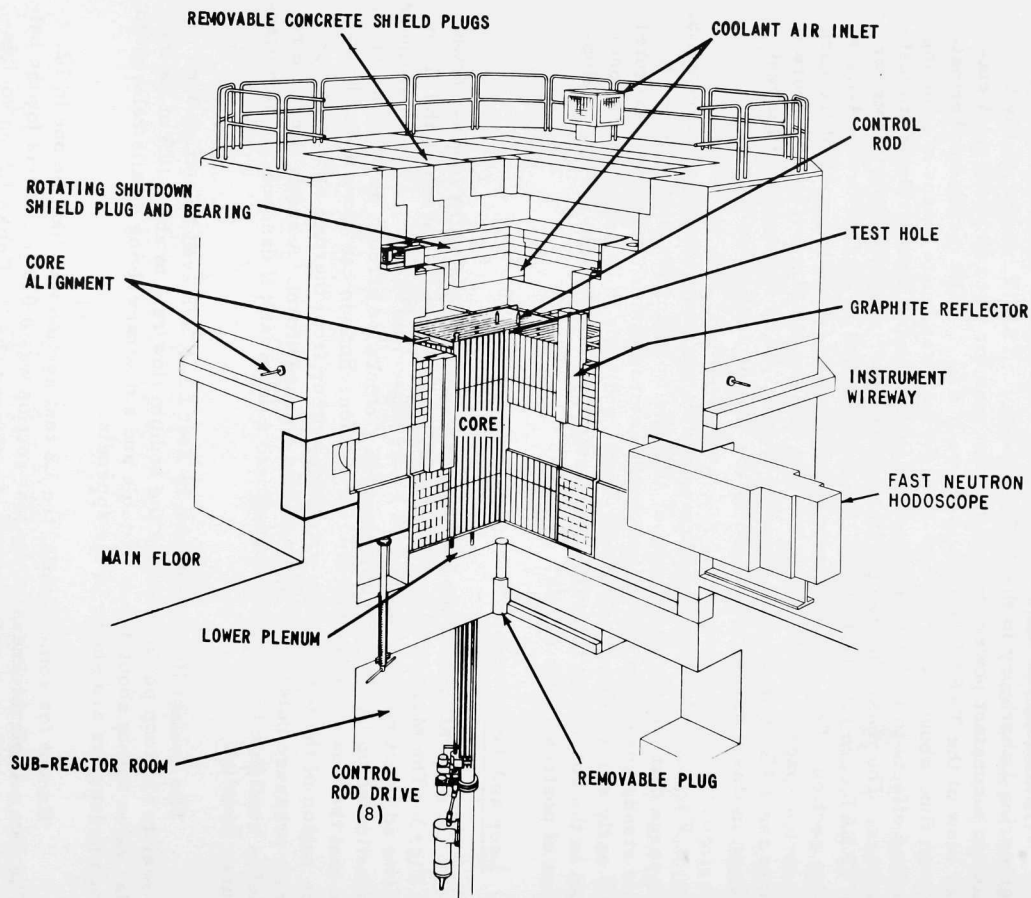


Fig. 1. Cutaway View of TREAT Facility. ANL Neg. No. 900-2776.

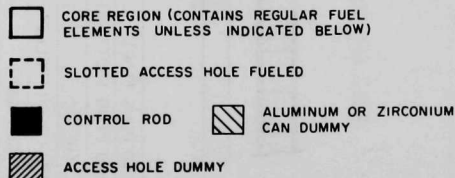
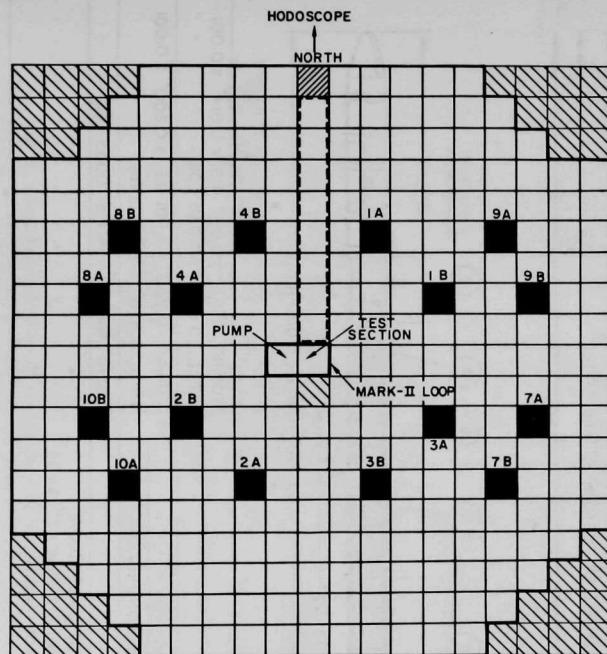


Fig. 2. TREAT Core-loading Diagram for Test L3.  
ANL Neg. No. 900-3591 Rev. 1.

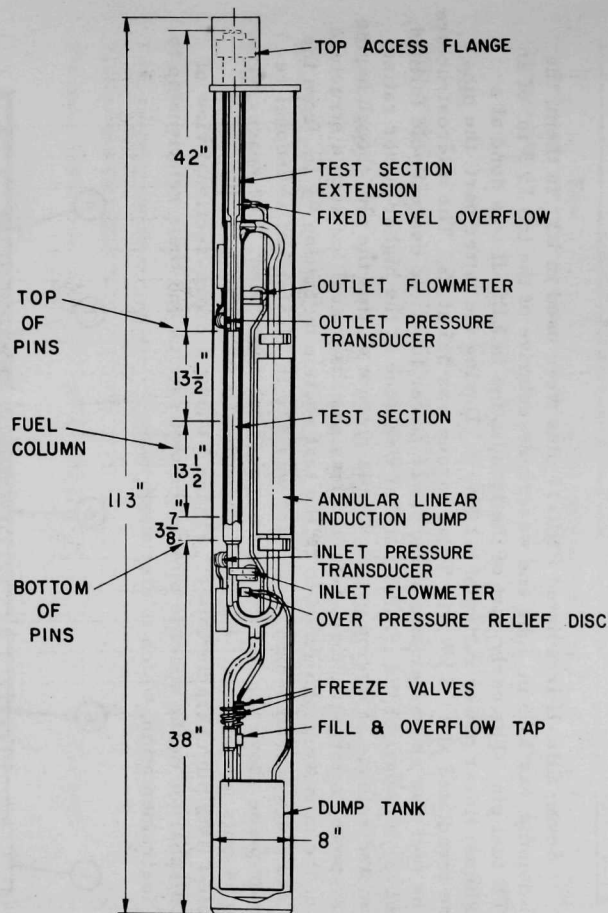
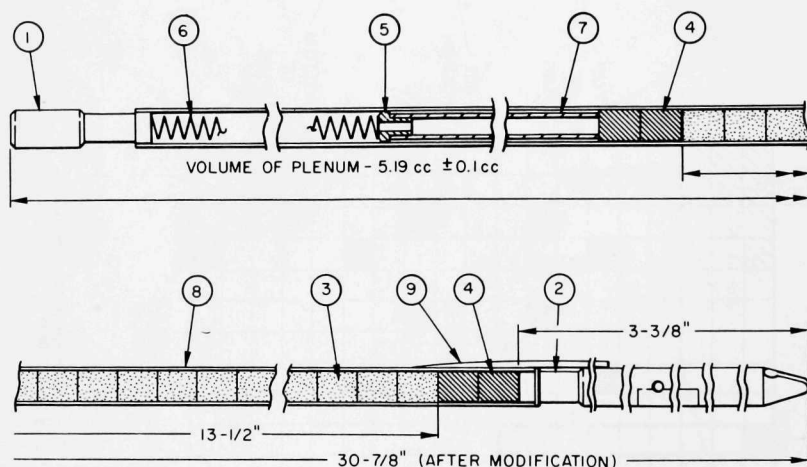


Fig. 3. General View of Test Section and Mark-IIA Loop.  
ANL Neg. No. 900-2777.

### C. Fuel Pins

Seven EBR-II irradiated PNL-17 pins were used in L3. In them, the fuel column was 13.5 in. long and was representative of the top 13.5 in. of an FFTF fuel pin. The early part of the irradiation in EBR-II was done at a maximum linear power rating of 9.2 kW/ft. During the latter part, the pins were irradiated at 11.5 kW/ft. Total burnup was 3.5 at. %. The microstructure of the fuel was characteristic of the lower power level; no central void formed. However, the part of the irradiation that was done at the higher power rating promoted release of fission gas to the pin plenum so that the pin, though having a low-power microstructure, retained less gas than usual for such a structure. Also, the pins were shortened to fit the test section by cutting  $9\frac{3}{8}$  in. from the top end plug; overall length of the pins was  $30\frac{7}{8}$  in. Instead of an Inconel reflector piece above the fuel column a spacer tube was used. The spacer wire was 54 mils in diameter. Figure 4 gives details of the PNL-17 pins, and Table I lists pin characteristics. Figure 5 shows a cross-sectional view of the disposition of the specific pins in the test section and their relationship to the instrumentation, which is discussed next.



1	END PLUG (TOP)	7	TUBING, 0.187" $\pm$ 0.002 O.D. $\times$ 0.014" $\pm$ 0.001 WALL, 5.937" $\pm$ 0.032 LONG
2	END PLUG (BOTTOM)	8	TUBING, 0.230" $\pm$ 0.001 O.D. $\times$ 0.200" $\pm$ 0.001 I.D. $\times$ 26.875" $\pm$ 0.016 LONG
3	FUEL	9	SOLID WIRE 0.0540" $\pm$ 0.0005 DIA.
4	INSULATOR PELLETS 0.25 LONG (EACH)		
5	SPACER CAP		
6	SPRING, COMPRESSION, 112 COILS, 0.194" $\pm$ 0.002 O.D., 0.025" $\pm$ 0.001 DIA. WIRE, 7" $\pm$ 1/32 FREE LENGTH, GRIND ENDS SQUARE.		

Fig. 4. Details of PNL-17 Fuel Pin



TABLE I. PNL-17 Fuel-pin Characteristics

Fuel	Irradiated Pins	Fresh Pins
Composition	75 wt % $\text{UO}_2$ 25 wt % $\text{PuO}_2$	75 wt % $\text{UO}_2$ 25 wt % $\text{PuO}_2$
Burnup	3.5 at. %	0
Enrichment	~61.6% $^{235}\text{U}$ in U 83.3% $^{239}\text{Pu}$ in Pu	65% $^{235}\text{U}$ in U 89% ( $^{239}\text{Pu}$ + $^{241}\text{Pu}$ in Pu)
Pellet density	Two or three restructured regions of different densities	10.34 g/cm <sup>3</sup> (93% TD)
Smear density	9.73 g/cm <sup>3</sup> (87.5% TD)	9.73 g/cm <sup>3</sup> (87.5% TD)
Pellets, ID, in.	0-0.003	0
OD, in.	0.195-0.199	0.194
Length, in.	13.5	13.5
Fuel-cladding diametral gap, in.	~0.006-0.004	0.006
Fission-gas retention, %	~51	0
Plenum pressure, psi	81 at 25°C	14.7 at 24°C
<u>Cladding</u>		
Type	20% cold-worked, Type 316 SS irradiated to 25,000 MWd/t	20% cold-worked Type 316 SS
Wall, in.	0.015	0.015

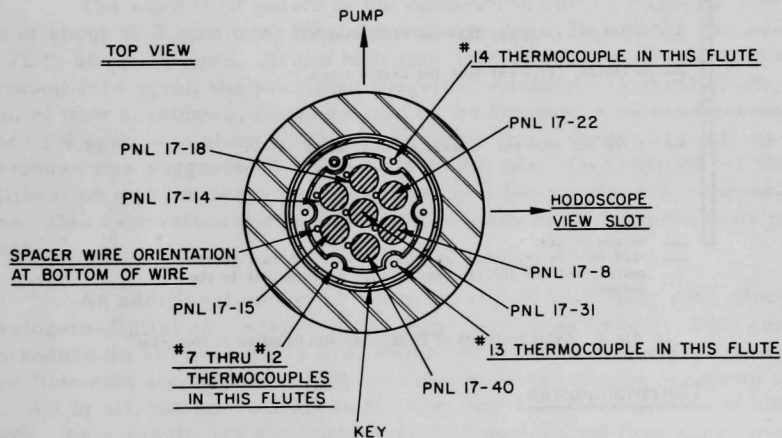


Fig. 5. Cross-sectional View of Arrangement of Fuel Pins and Instrumentation

## D. Instrumentation

The Mark-II loop of Test L3 was fitted with upper and lower flowmeters, and upper and lower pressure transducers, as shown in Fig. 2. Fourteen thermocouples (hereafter designated TC1, TC2, etc.) were situated along the test section. Figure 6 indicates their locations.

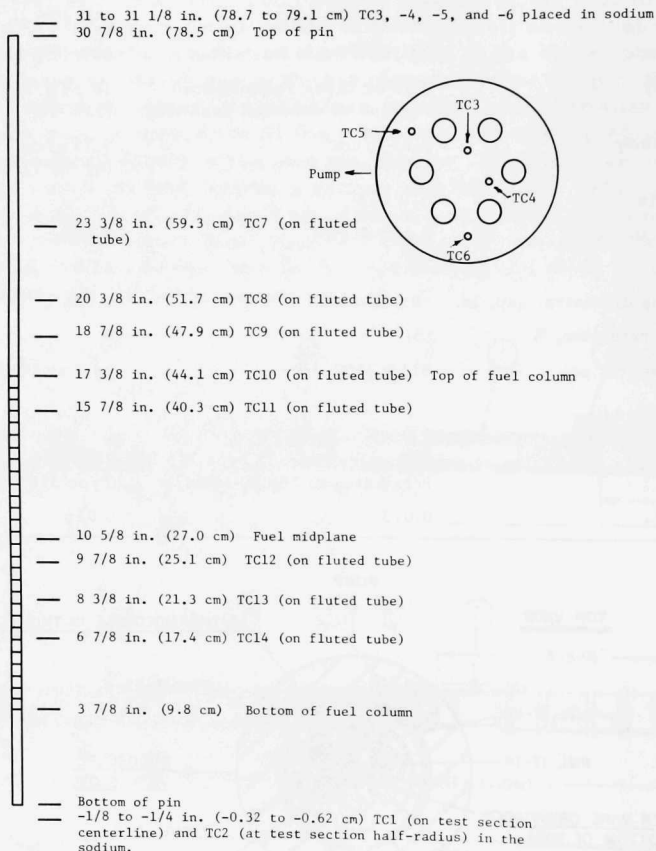


Fig. 6. Axial Positions of Thermocouples Relative to Fuel Pins

### 1. Thermocouples

The junctions of thermocouples TC1 and TC2 were located in the inlet sodium just below the bottom of the test section. The junctions of thermocouples TC3-TC6 were in the outlet sodium, approximately in a plane 1/8 to

1/4 in. above the top end of the fuel pins, about even with the upper pressure-transducer port. These six thermocouples measured sodium temperatures directly. The junctions of the eight remaining thermocouples were welded to the outside of the fluted tube at various points and measured structure temperatures. TC10-TC14 measured structure temperatures adjacent to points on the fuel column. TC7-TC9 were welded to spots on the fluted tube above the tops of the pins.

In the performance of the experiment, it became evident that the outputs from TC2 (in the inlet sodium) and TC3 (in the outlet sodium) were essentially the same. Subsequently, TREAT personnel discovered a cross connection in the wiring of these thermocouples in the instrument console. This situation left TC1 as the indicator of inlet-sodium temperature. Also, TC6 proved to be nonfunctional, so that with the loss of TC3, only TC4 and TC5 were available to record the temperature of outlet sodium. Among the structure thermocouples, TC13 and TC14 failed early in Run 2. This left TC10-TC12 to measure structure temperatures adjacent to the upper half of the fuel column in the crucial parts of the experiment during and after coastdown.

## 2. Flowmeters

The flowmeters were standard Mark-IIA loop instruments. The lower flowmeter was calibrated with orifices during loop preparation. The upper flowmeter was then calibrated against the lower one before the experiment. During this intercalibration, the sodium was flowing at the pretest temperature. The calibration factors were 11.32 gpm/mV for the lower flowmeter and 27.76 gpm/mV for the upper one.

The scatter of points in the calibration curves suggests a precision of about  $\pm 0.2$  gpm over the calibration range. This range extended from about 22 to about 2.8 gpm. At the high flow rate prevailing at the start of the experiment ( $\sim 14$  gpm), the precision therefore amounted to about  $\pm 1.4\%$ . After the end of flow coastdown, the precision in the flowmeter measurements (for flow of  $\sim 1.4$  gpm) was about  $\pm 14\%$ . Some dependence of the calibrations on temperature was suggested in an earlier study; the effect noticed for the L3 calibration was not large enough to justify a temperature-dependent calibration. One calibration curve was taken to apply at all temperatures of interest.

An additional aspect of the accuracy of flowmeter data concerns the analog-to-digital conversion of the data (discussed below). This conversion can introduce an error of  $\pm 0.05$  mV, which for the 0.18-mV signal typical of the low flow rate amounted to  $\pm 28\%$  uncertainty in the values for these flow rates. All in all, the uncertainty in the low flow rates can amount to about  $\pm 30$ -40%. As a result, the flowmeters served best at low flow rates as semi-quantitative indicators of flow in order to assess the times of start of boiling and other flow-disruptive events. A quantitative treatment, such as integration of flow over longer than a fraction of a second in order to provide an estimate of void size and growth, is uncertain.

### 3. Pressure Transducers

The pressure transducers were of an unbonded strain-gauge type and were located above and below the test section, as shown in Fig. 3. Pressures reported below in the data graphs are not absolute pressures, but are pressures relative to the prevailing loop pressure at the start of the run when the pressure transducers were electronically zeroed.

The pressure transducers were high-pressure-range instruments (2500 psi) in order to meet safety-dictated strength requirements, since they provided part of the loop closure. Generally, the accuracy of any instrument at the low end of its operating range is worse than at its high end. For these pressure transducers, which were required to produce data for low pressure, the accuracy was estimated to be  $\pm 30$ -35 psi. Furthermore, the accuracy can be expected to have deteriorated as the run progressed because of shifts in the zero point of the instruments.

One cause for the shifts was the temperature dependence of the instruments, which was revealed by experience to be present despite efforts by the manufacturer to provide temperature compensation. Effects of the radiation field on these strain-gauge devices were also nonreproducible from unit to unit, but appeared to be small for the L3 transducers. At their present stage of development and application, the pressure transducers are probably best regarded as indicators of the timing of abrupt pressure changes and of the approximate magnitudes of these changes.

### 4. Hodoscope

The hodoscope is a device that records fuel positions by means of fast neutrons emitted by fissioning fuel atoms. Basically, the instrument consists of an array of 334 collimating channels, each aimed at a given region of the test section. Fission neutrons emerging from such a region are detected and counted. Coolant and structural elements are essentially transparent to the fast neutrons ( $>2$  MeV) that contribute to the hodoscope image. The counts-per-channel data are recorded as a function of time and are later analyzed. This analysis can yield a graphical display of fuel position as a function of time, or it can be used to give a dynamic display, on an oscilloscope, of sequences of images of fuel position. Further processing into a motion-picture reconstruction of the events is also possible. Whatever the mode of data analysis, the hodoscope gives a two-dimensional view of three-dimensional events. The pump is located to the right in this plane, as seen from the hodoscope.

## III. TEST L3, RUN 1

A. General Description and Data Graphs of Run 1

Two runs comprised Test L3. The first run, designated L3-1 or L3-Run 1, was TREAT transient number 1482 and was performed on December 21, 1972, at 1228 hours. Test L3-1 was performed with a reactor power transient, described in Fig. 7, but without a flow coastdown. Other data for L3-1 are presented in Figs. 8-15.

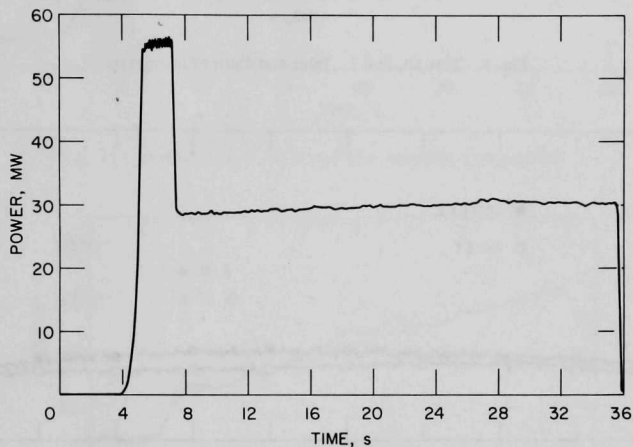


Fig. 7. Test L3, Run 1: Reactor Power

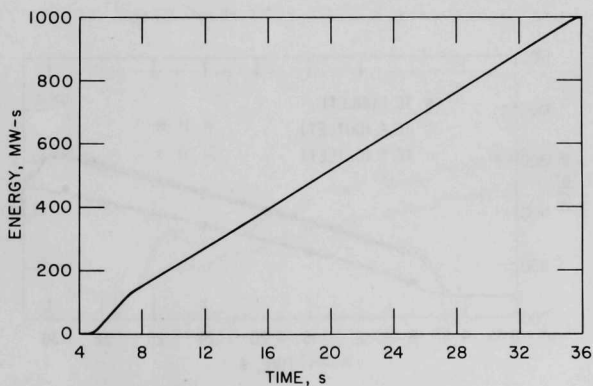


Fig. 8. Test L3, Run 1: Integrated Reactor Power

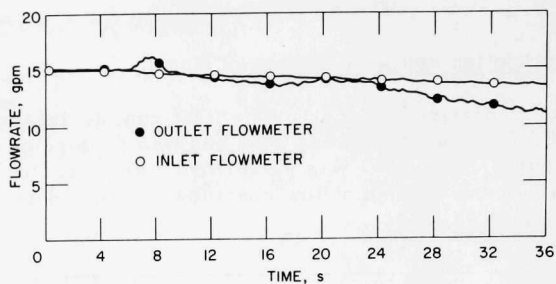


Fig. 9. Test L3, Run 1: Inlet and Outlet Flowmeters

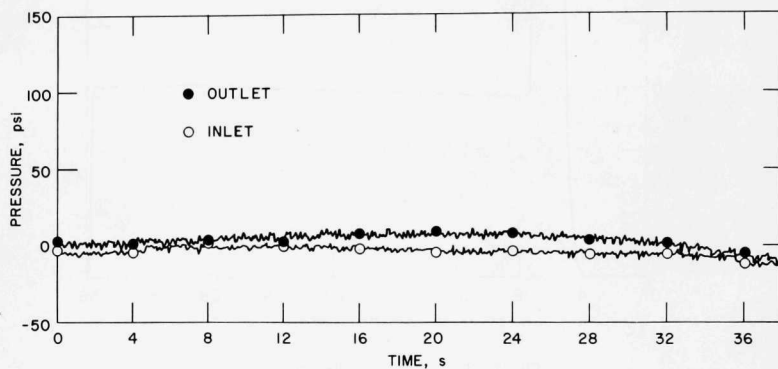


Fig. 10. Test L3, Run 1: Inlet and Outlet Coolant Pressure

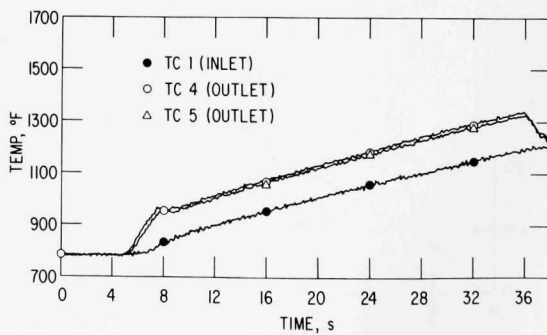


Fig. 11. Test L3, Run 1: Inlet and Outlet Coolant Temperature

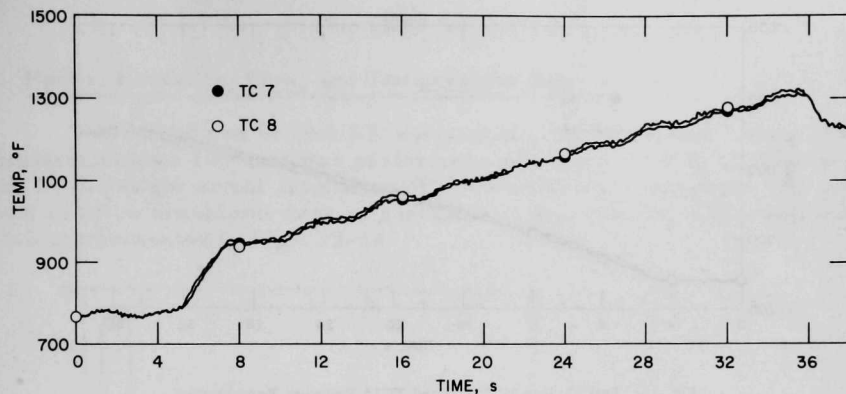


Fig. 12. Test L3, Run 1: TC7 and TC8 Structure Temperature

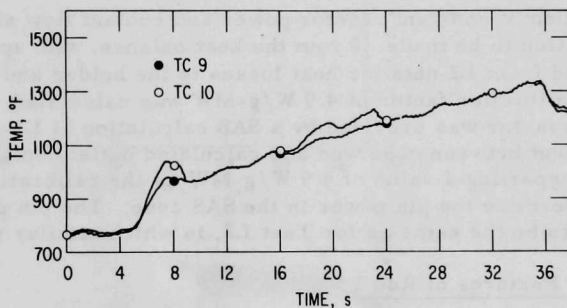


Fig. 13. Test L3, Run 1: TC9 and TC10 Structure Temperature

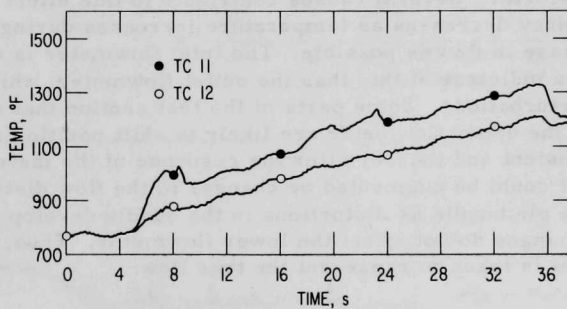


Fig. 14. Test L3, Run 1: TC11 and TC12 Structure Temperature



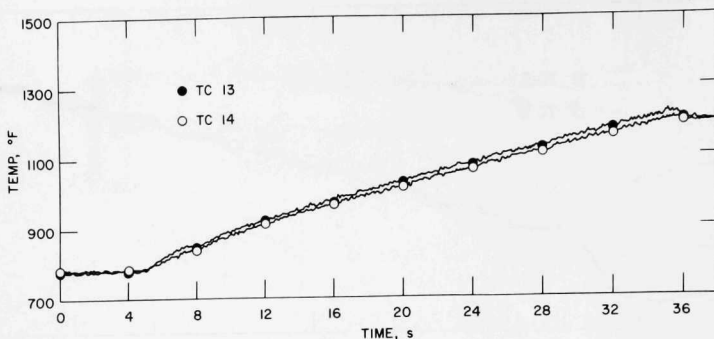


Fig. 15. Test L3, Run 1: TC13 and TC14 Structure Temperature

### B. Calibration Factor for Test L3

The period of constant reactor power and coolant flow allowed a heat-balance calculation to be made. From the heat balance, with appropriate corrections derived from L2 data for heat losses to the holder and to upper parts of the pins, a calibration factor of 4.9 W/g-MW was calculated. A check on this calibration factor was provided by a SAS calculation of L3-Run 1. Satisfactory agreement between observed and calculated outlet coolant temperatures was taken as supporting a value of 4.9 W/g-MW as the calibration factor that was used to determine the pin power in the SAS code. The pin power distribution was taken to be the same as for Test L2, in which similar pins were used.

### C. Noteworthy Features of Run 1

An apparent decline in flow rate as indicated by both flowmeters is typical of the L-series experiments. An apparently more gradual decline is shown by the inlet flowmeter. Several causes contribute to this effect. For one, since the pump efficiency decreases as temperature increases during the transient, a genuine decrease in flow is possible. The inlet flowmeter is expected to be a more accurate indicator of this than the outlet flowmeter, which is subject to a number of perturbations. Some parts of the test section that are in the magnetic circuit of the upper flowmeter are likely to shift position slightly in the course of a transient and thereby alter the response of the instrument. Such a calibration shift could be augmented by changes in the flow distribution at the outlet end of the pin bundle as distortions in the bundle develop during the transient. These changes do not affect the lower flowmeter. Thus, the lower-flowmeter signal is taken to represent the true flow.

A noticeable feature of the structure-thermocouple readouts is a slow oscillation superimposed on the expected general rise in temperature throughout the transient. This oscillation is present even before the beginning of heating. Though unexplained, this effect does appear most pronounced for TC8 and decreases going down the tube, being gone for TC13 and TC14, the thermocouples adjacent to the lower part of the fuel column.

## IV. TEST L3, RUN 2

A. Power, Pressure, Flow, and Temperature Data

The second run in Test L3, designated L3-2 or L3-Run 2, was TREAT transient number 1483 and was performed on January 2, 1973, at 1658 hours. Run L3-2 was the actual simulation of a flow-coastdown accident. The power level and flow coastdown were as described in Figs. 16-18. Other data for L3-2 are presented in Figs. 19-34.

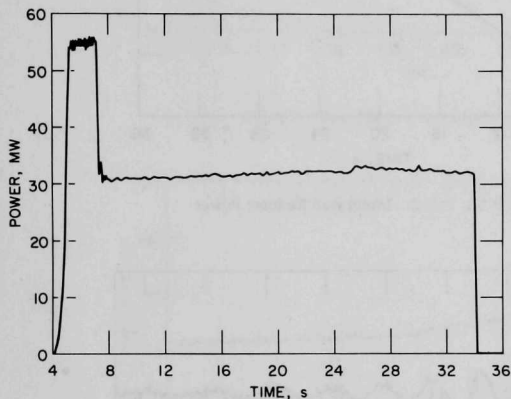


Fig. 16

Test L3, Run 2: Reactor Power

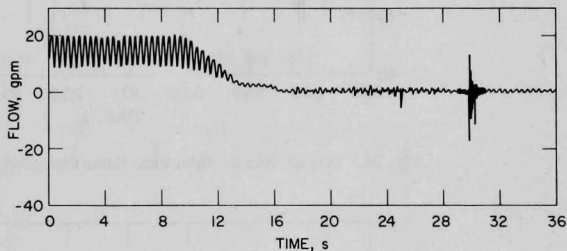


Fig. 17

Test L3, Run 2: Inlet Flow Rate

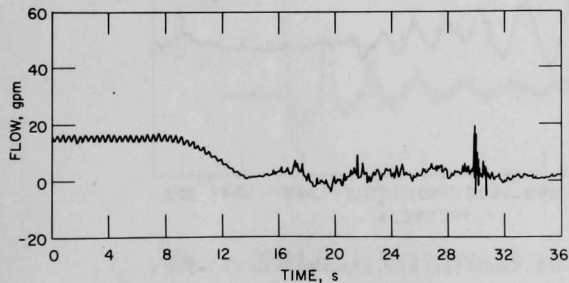


Fig. 18

Test L3, Run 2: Outlet Flow Rate

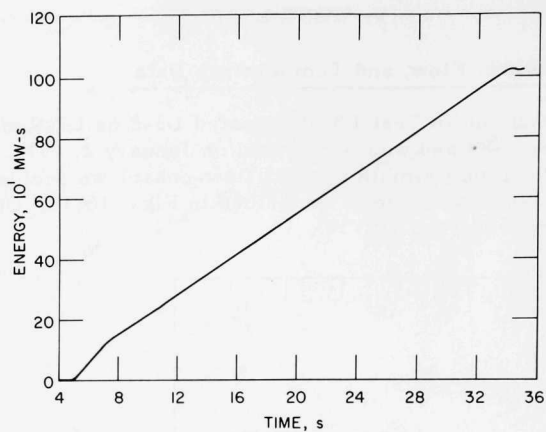


Fig. 19. Test L3, Run 2: Integrated Reactor Power

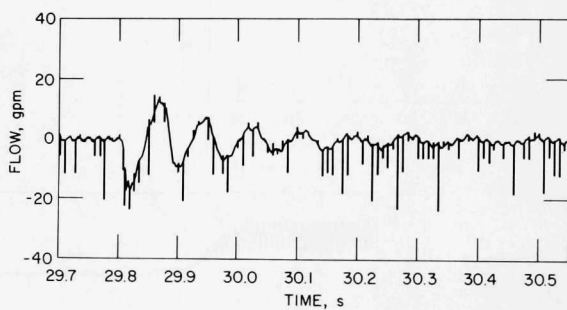


Fig. 20. Test L3, Run 2: Inlet Flow Rate; Expanded Scale 29.7-30.5 s

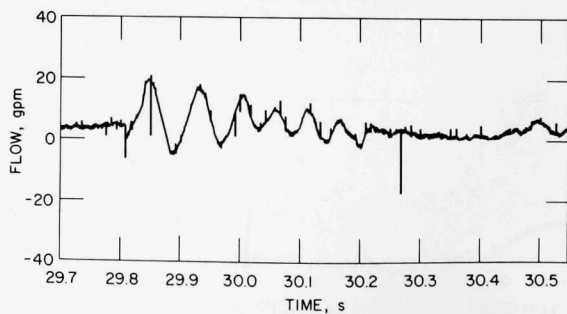


Fig. 21. Test L3, Run 2: Outlet Flow Rate; Expanded Scale 29.7-30.5 s

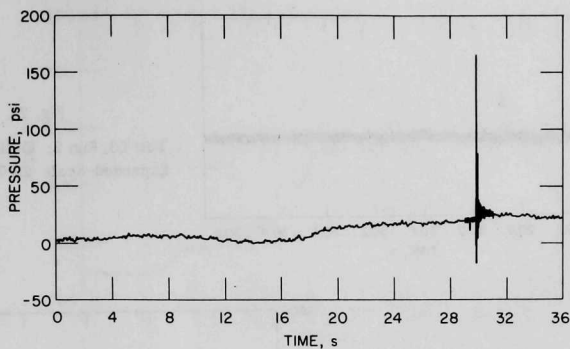


Fig. 22. Test L3, Run 2: Inlet Pressure

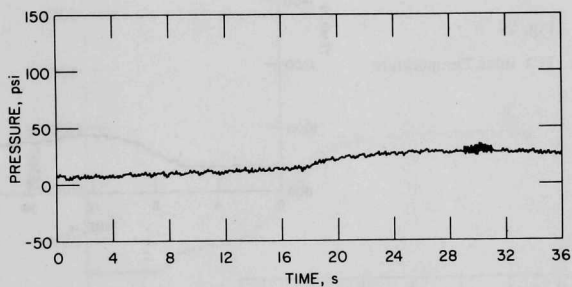


Fig. 23. Test L3, Run 2: Outlet Pressure

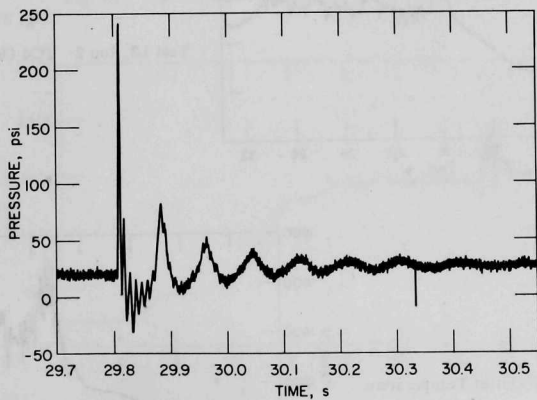


Fig. 24. Test L3, Run 2: Inlet Pressure; Expanded Scale 29.7-30.5 s

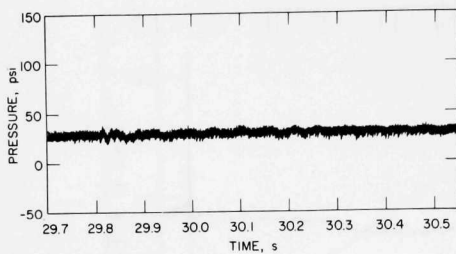


Fig. 25

Test L3, Run 2: Outlet Pressure;  
Expanded Scale 29.7-30.5 s

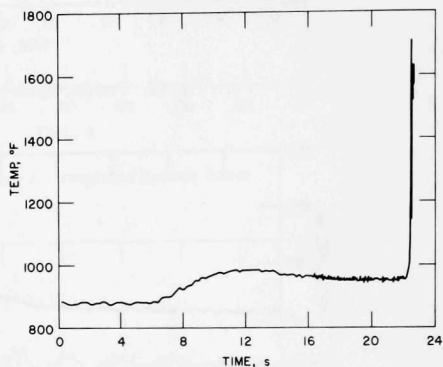


Fig. 26

Test L3, Run 2: TC1 Inlet Temperature

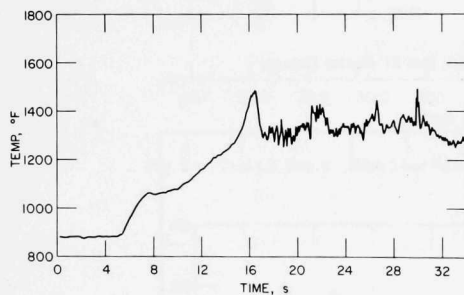


Fig. 27

Test L3, Run 2: TC4 Outlet Temperature

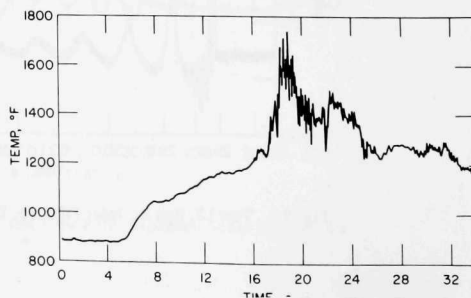


Fig. 28

Test L3, Run 2: TC5 Outlet Temperature

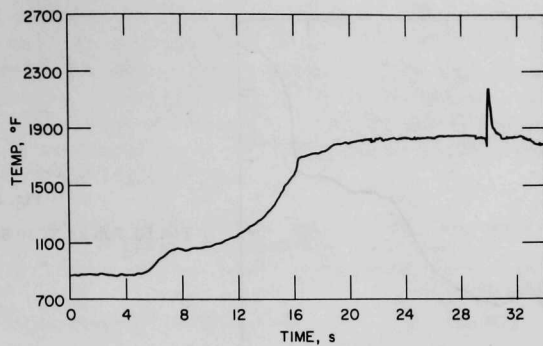


Fig. 29. Test L3, Run 2: TC7 Structure Temperature

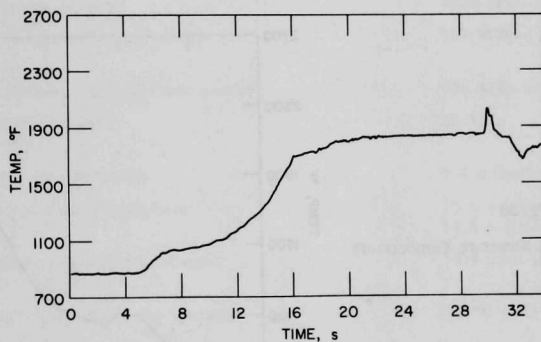


Fig. 30. Test L3, Run 2: TC8 Structure Temperature

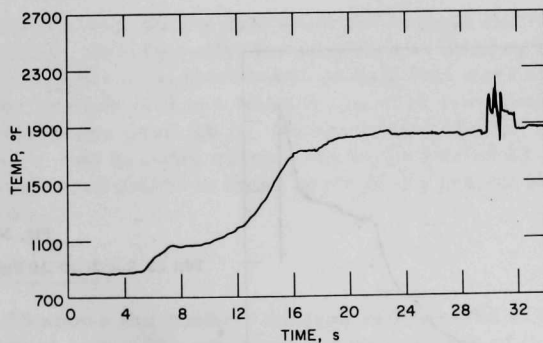


Fig. 31. Test L3, Run 2: TC9 Structure Temperature

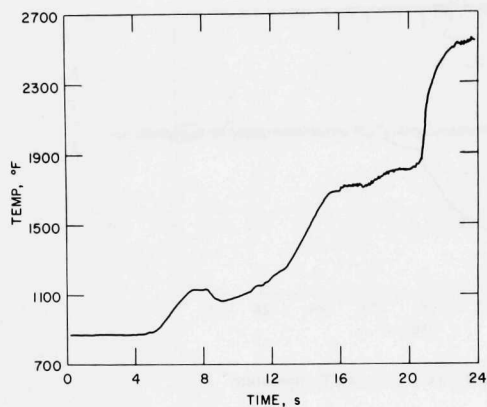


Fig. 32

Test L3, Run 2: TC10 Structure Temperature

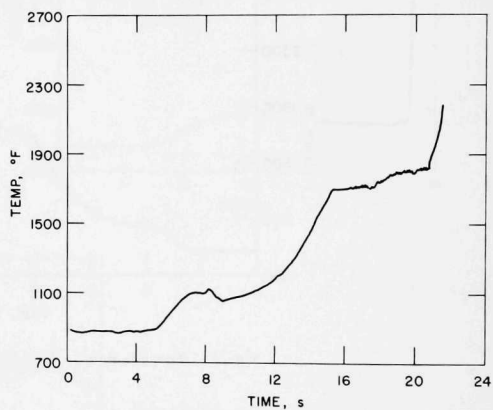


Fig. 33

Test L3, Run 2: TC11 Structure Temperature

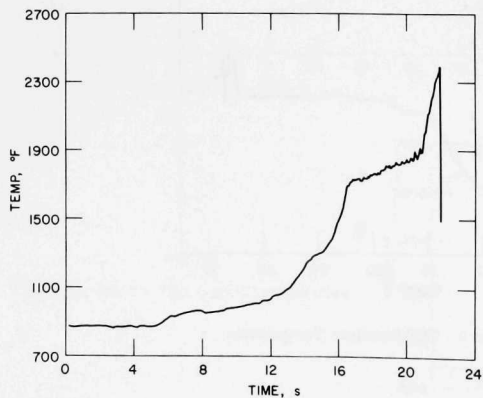


Fig. 34

Test L3, Run 2: TC12 Structure Temperature



Table II presents various experimental parameters as they were established or observed. An average TREAT power of 31.5 MW was taken from observations during the sustained power part of the experiment in order to calculate the specific power of 155 W/g. If the calibration factor, also termed the test-pin-to-reactor-power coupling, is to be expressed in units of W/cm<sup>3</sup>-W reactor power, it would be, for a pellet density of 10.34 g/cm<sup>3</sup> (93% of theoretical density),  $5.06 \times 10^{-5}$  W/cm<sup>3</sup>-W.

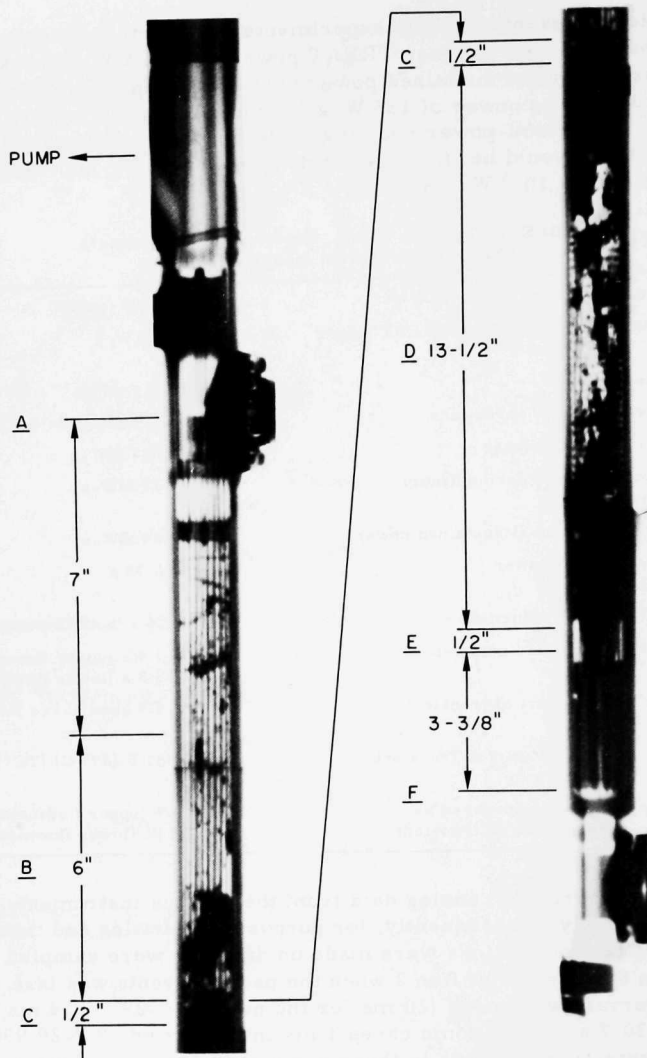
TABLE II. Test L3, Run 2: Experimental Parameters  
(Observed or derived from observation)

Calibration factor	4.9 W/g-MW
Specific power during sustained TREAT power (31.5 MW)	155 W/g
Average linear power	9.27 kW/ft
Total energy release in seven pins	2.37 MW-s (= $2.37 \times 10^6$ J)
Total reactor energy release	1027 MW-s
Reactor energy release during heatup (up to 7.25 s)	127 MW-s
Reactor energy release at sustained power	900 MW-s
Duration of sustained power (7.25 to 34.0 s)	26.75 s
Time at start of flow reduction	9.4 s (both flowmeters)
Time when flow reduction complete	13.4 s (upper flowmeter) 13.8 s (lower flowmeter)
Coolant flow rate at start of transient (5.25 s)	14.4 gpm (lower flowmeter)
Coolant temperature at start of transient (5.25 s)	883°F (473°C) (TC1)
Reduced flow at 14.6 s; expressed as percentage of flow at start of transient	6% (upper flowmeter) 14% (lower flowmeter)

In the experiment, analog data from the various instruments were recorded continuously. Subsequently, for purposes of plotting and tabulation, analog-to-digital conversions were made on data that were sampled at 200-ms intervals. In the periods of Run 2 when the pace of events was fast, shorter sampling intervals were used (20 ms for the period 15-29.7 s, 4 ms for the period 29.7-30.7 s, and in some cases 1 ms in the period 29.7-29.990 s). A denser concentration of points in these parts of the graphs is due to this more frequent sampling.

## B. Neutron Radiographs

Figure 35 shows the posttest neutron radiographs of the test-section side of the stripped loop. The most prominent features of these radiographs are (1) the extensive removal of fuel from the midregion of the column and



A - TOP OF PINS  
 B - SPACER TUBE  
 C, E - INSULATOR PELLETS

D - ORIGINAL FUEL COLUMN  
 F - BOTTOM OF PINS

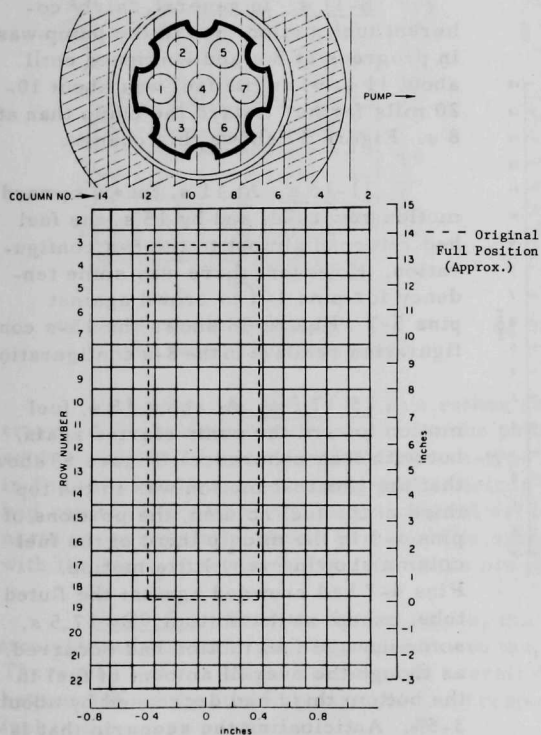
Fig. 35. Posttest Neutron Radiograph of Test L3. ANL Neg. No. 900-76-577.

(2) the displacement of fuel upward past the original top of the column. The bulk of the fuel that was displaced upward out of the original fuel region was concentrated in the space of 3 in. above the top of the column. Numerous small splatters came to rest above this region. The three largest ones were centered  $4\frac{1}{4}$ , 6, and  $8\frac{3}{8}$  in. above the original top of the fuel. About 10-12 in. above the top of the column, some transverse, slanting streaks were seen. These came from wires (instrument leads) that spiraled around the test section and around which fuel was caught.

Since the region from the original top of the column down to a level about  $2\frac{1}{4}$  in. below the top appears as a solid zone of fuel in the radiographs, and since fuel did move up out of the column, it follows that fuel was displaced to fill in this region at the top of the column from the voided central region.

According to the radiograph, the bottom 4 in. of the fuel column contained a few small voids. Some fuel movement apparently occurred in this

region, but the amount was relatively small compared to that involved in the upward movement. Probably the explosive forces, while mainly moving fuel upward, also impelled some downward.



### C. Hodoscope Results

The reduced hodoscope data are presented in an array of rows and columns as shown in Fig. 36. The relative position of the test section on the array is shown, as well as the coverage of the pins by the respective columns of neutron detectors. Each channel of the hodoscope covers a spatial element  $0.15 \times 0.875$  in., so that the square representation of channels in Fig. 36 is schematic and must be interpreted in accord with the designated inch scales. For ease of reference, the pins have been assigned simple numbers as shown, and the correspondence is #1 = PNL-17-40,

Fig. 36. Hodoscope Channels in Relation to Test Section

#2 = PNL-17-15, #3 = PNL-17-8, #4 = PNL-17-31, #5 = PNL-17-14, #6 = PNL-17-22, and #7 = PNL-17-18 (see also Fig. 5).

The initial fuel motion, starting as early as during the preheat phase, consisted of coherent motion of the entire fuel bundle toward the pump. Incoherency developed as the temperature rose. Details of the progress of fuel motion are described in the following time steps.

5-7.5 s. Nonlinearity of the detectors precludes precise interpretation of the hodoscope data during the preheat period. However, since fuel motion

was evidently in progress at the very beginning of the immediately following power-plateau period, it seems reasonable to assume that there was some fuel motion during the preheat period.

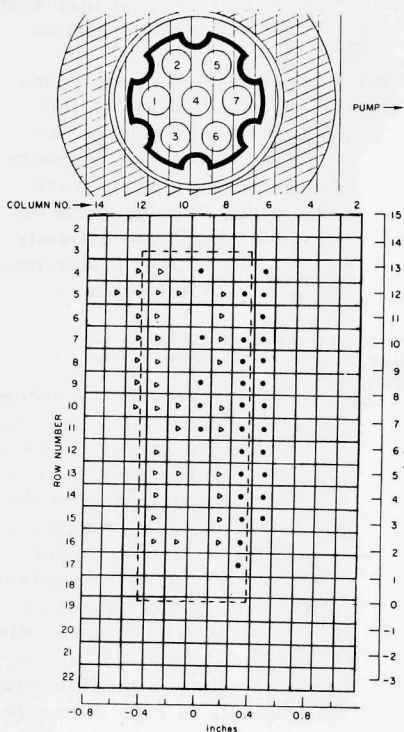


Fig. 37

Test L3 Fuel Configuration at 11 s with Respect to 8-s Configuration. (A solid circle represents an increase over the initial signal in the hodoscope channel, and a hollow triangle indicates a decrease. The larger the symbol, the greater the change.)

8-11 s. In general, fairly coherent fuel motion toward the pump was in progress at 8 s and continued until about 11 s, when the fuel was about 10-20 mils farther toward the pump than at 8 s. Figure 37 shows this change.

11-15 s. At 11 s, the pumpward motion reversed, and by 15 s, the fuel had returned almost to the 8-s configuration. However, there was some tendency for pins 1-4 to crowd against pins 5-7. Figure 38 shows the 15-s configuration relative to the 8-s configuration.

15-17.5 s. At about 15 s, fuel motion toward the pump started again, but with less coherence. Figure 39 shows that the greatest motion was in the top third of the fuel column, the portions of pins 1-3 in the middle third of the fuel column showing very little motion. Pins 4-7 had crowded against the fluted tube, except at the bottom. By 17.5 s, some upward fuel motion had occurred, as though the overall amount of fuel in the bottom third had decreased by about 3-5%. Anticipating the scenario that is presented later in this report, we note that this interval covers the start of boiling, the start of cladding dryout, and the start of cladding melting, as predicted by SAS.

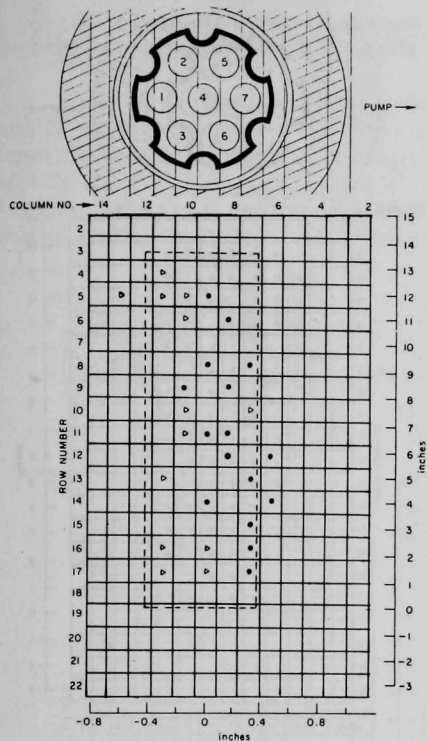


Fig. 38. Test L3 Fuel Configuration at 15 s with Respect to 8-s Configuration

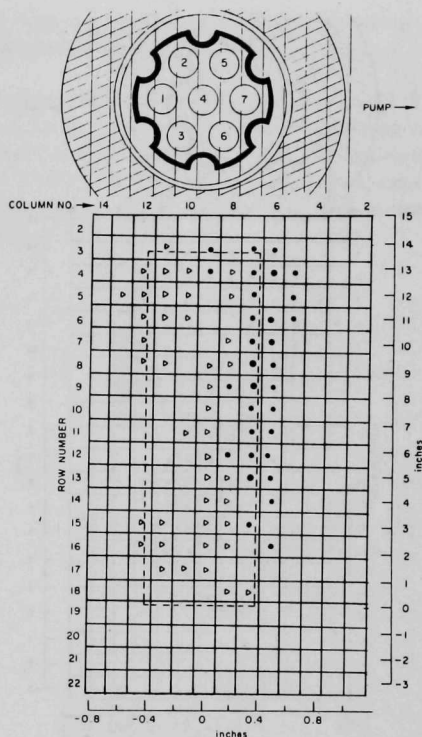


Fig. 39. Test L3 Fuel Configuration at 17.5 s with Respect to 8-s Configuration

17.5-19 s. At about 17.5 s, a rather sharp reversal occurred in the travel of the midportion of the pins on the pump side. The pins had started to squirm, and at 19 s had acquired a wave-type or spiral distortion, as shown in Fig. 40. At 19 s, the overall fuel deficit in the lower third of the fuel region had returned to within  $\sim 1\%$  of its original value. In this time period, the scenario appearing later shows that there is experimental evidence consistent with the start of release of gas from the pin plenums.

19-20.5 s. Between 19 and 20.5 s, the lower half of the fuel pins straightened out (at least perpendicular to the line of sight of the hodoscope). There was again a slight decrease in overall density and amount of fuel in the bottom 40% of the fuel column, and a corresponding increase in the amount of fuel in the upper portion.

The situation at 20.5 s is shown in Fig. 41. A persistent feature up to this time was a depletion by 20-30% of the fuel in the upper corner away from the pump. The top quarter of the fuel column evidently remained displaced toward the pump.

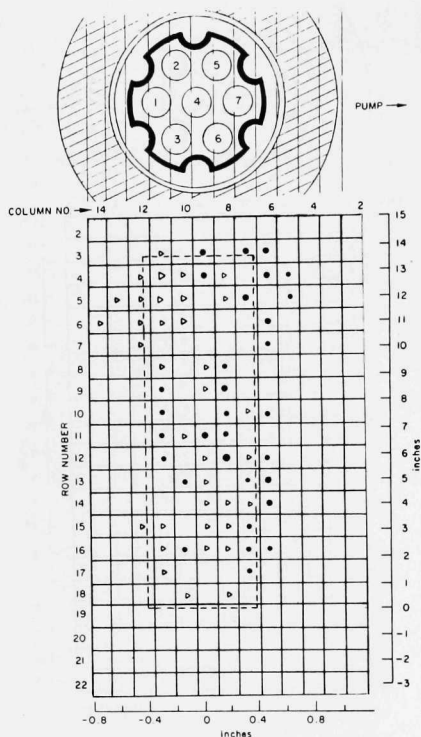


Fig. 40. Test L3 Fuel Configuration at 19 s  
with Respect to 8-s Configuration

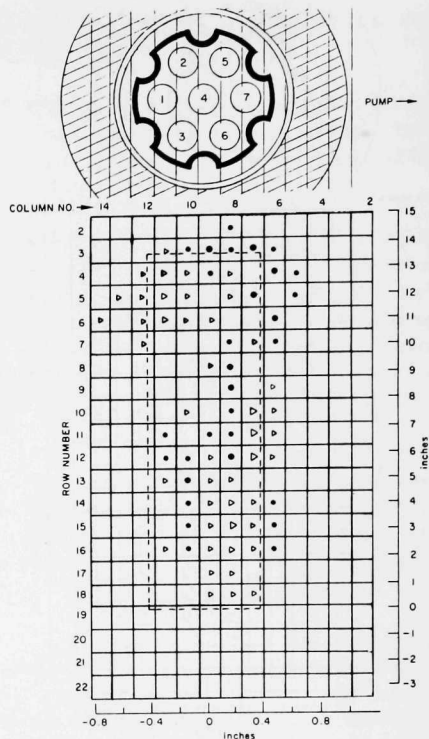


Fig. 41. Test L3 Fuel Configuration at 20.5 s  
with Respect to 8-s Configuration

At 19.8 s, the SAS calculation predicted structure dryout to start in the region about 2 in. above the fuel midplane.

20.5-22 s. By 22 s, the fuel pins had lost most of their geometrical integrity and seemed to be moving as pellets or fragments rather than as columns. Figures 42 and 43 show the 22-s configuration, compared to the 8- and 20.5-s configurations, respectively.

Notable features of fuel motion in the 20.5-22-s period (see Fig. 43) are listed below.

a. An agglomeration of fuel fragments formed against the pump side of the fluted tube near the original fuel midplane. Fuel moved toward this region from below, from above, and, to a lesser extent, from the side opposite (i.e., away from) the pump.

b. Some fuel moved toward the upper corner away from the pump, thereby replenishing this previously depleted region.

c. A penetration of the fluted tube probably occurred between 21.5 and 22 s, on the pump side at Rows 9 and 10 (half to two-thirds of the way up from the bottom of the fuel column). The timing correlates with the failure of TC1 (22.7 s), TC12 (21.8-22.0 s), and TC11 (22.4 s). These failures could have resulted from meltthrough of the thermocouple leads in TC1 and from meltthrough of the TC12 and TC11 junctions and/or leads.

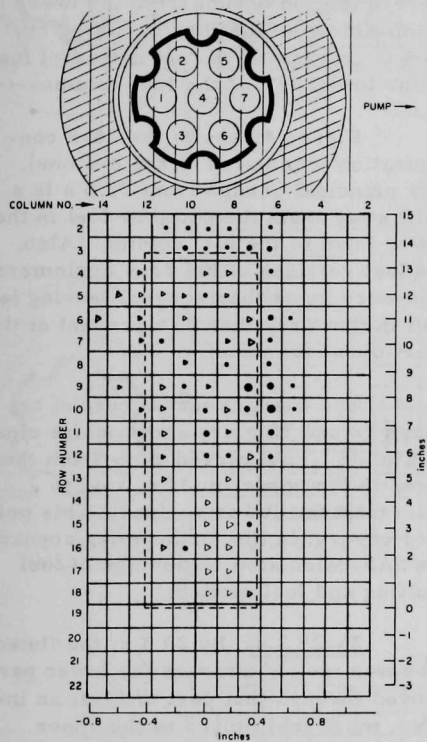


Fig. 42. Test L3 Fuel Configuration at 22 s with Respect to 8-s Configuration

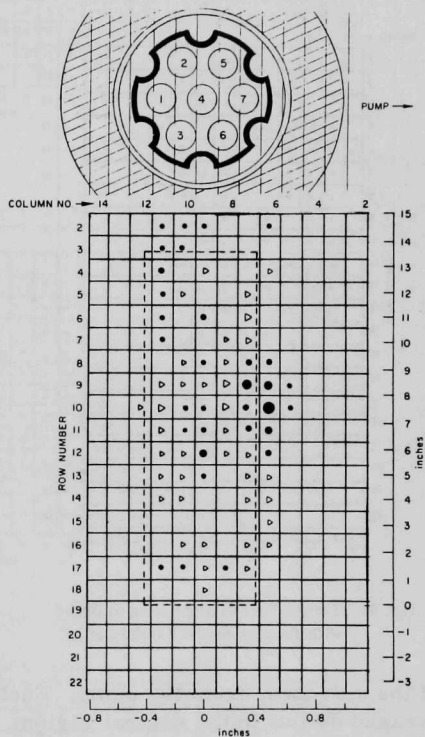


Fig. 43. Change in Test L3 Fuel Configuration between 20.5 and 22.0 s

The flute between pins 1 and 2 carried the leads and junctions for thermocouples TC7-TC12. At the time of failure of TC12 there was no event in the sense of fuel gain at Row 12 and columns 11 and 12, according to the hodoscope. However, pin 1 could have moved away from the hodoscope, contacted the flute, and melted through it. Such motion would not be detected by the hodoscope.



22-26 s. The midplane agglomeration at 22 s did not last long, having largely disappeared by 23.5 s, as shown by Fig. 44. Comparison of Figs. 42

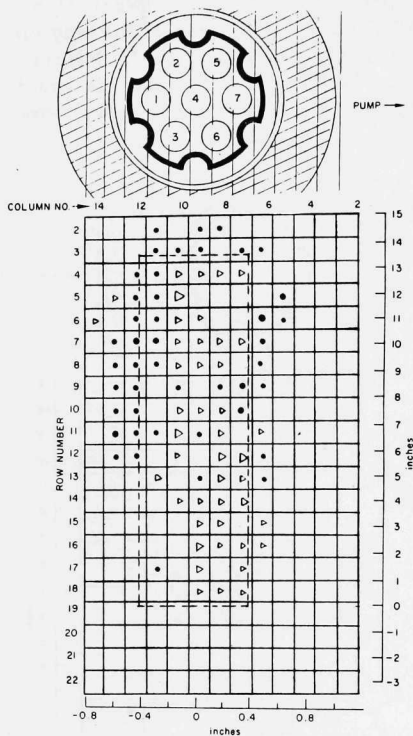


Fig. 44. Test L3 Fuel Configuration at 23.5 s with Respect to 8-s Configuration

and 44 shows that motion away from the pump had occurred in the upper two-thirds of the fuel column. In Rows 7-12, fuel pellets apparently had penetrated the fluted tube and were resting against the bellows portion of the outer can. Figures 42 and 44 also show that further upward motion of fuel from the lower pump-side quadrant had occurred by 23.5 s, increasing the net deficit of fuel in the lower 40% of the fuel column.

Figure 45 shows the 26-s configuration (compared to the 8-s one). The principal change from 23.5 s is a shift away from the pump by fuel in the lower third of the fuel column. Also, the last vestiges of the 22-s agglomeration were more than erased, leaving less fuel in that area than was present at the start of the transient.

The changes that occurred between 22 and 26 s are shown more clearly in Fig. 46. Fuel moved away from the pump to the upper, middle, and, to a lesser extent, lower regions. This period covers, in the forthcoming scenario, the SAS-calculated beginnings of fuel melting and fuel motion.

26-29.3 s. By 29.3 s, the fluted tube was melted away on the lower part of the side away from the pump. Fuel moved through that part and left an increased deficit in the central region. Also, more fuel moved to the upper part, away from the pump, through the fluted tube (see Fig. 47).

Up to this point, the hodoscope data can be explained on the basis of whole pellets or pellet fragments shifting around, but the data do not preclude molten fuel in the form of foam or in some other gas-supported condition.

Eruption at 29.8 s. A sudden voiding of the central region of the fuel began at 29.75 s and was largely completed within 150 ms. Figure 48 shows the change in the 260-ms interval between 29.72 and 29.98 s. Most of the fuel motion was upward, with  $10 \pm 2\%$  of the fuel disappearing above the viewing



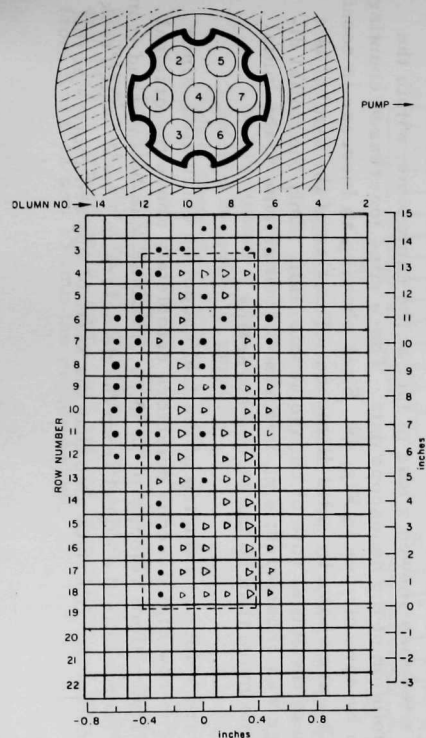


Fig. 45. Test L3 Fuel Configuration at 26 s with Respect to 8-s Configuration

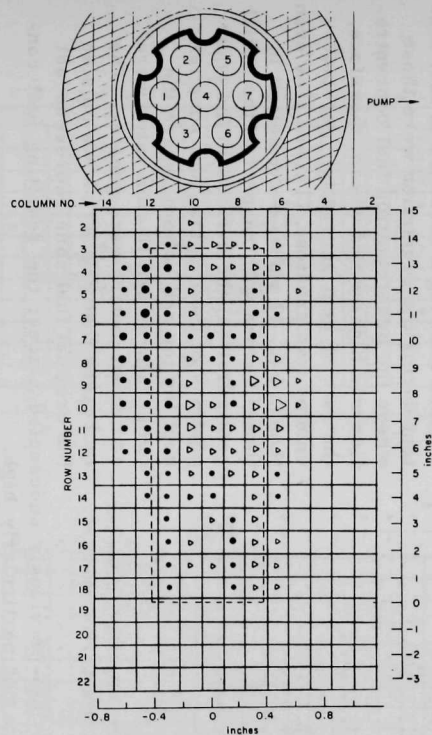


Fig. 46. Change in Test L3 Fuel Configuration between 22.0 and 26.0 s

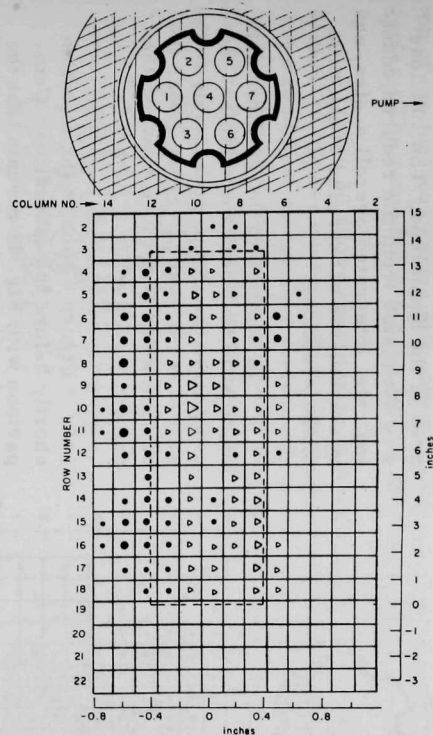


Fig. 47. Test L3 Fuel Configuration at 29.3 s with Respect to 8-s Configuration

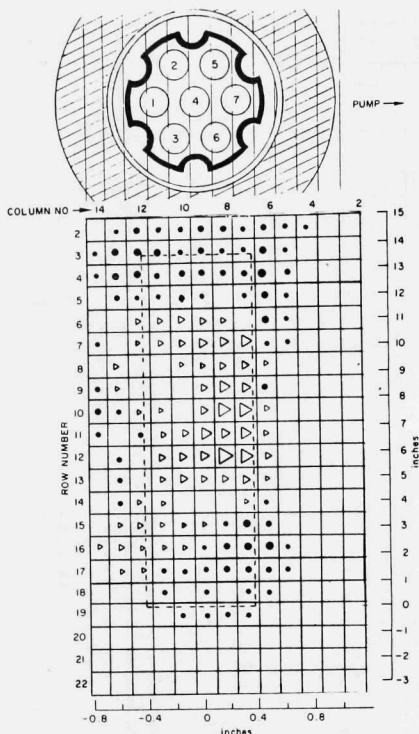


Fig. 48. Change in Test L3 Fuel Configuration due to Eruption between 29.72 and 29.98 s

that had moved into previously unoccupied places; the resulting fuel concentrations were not particularly high.

Several sites also showed a loss of fuel at the same time, within the  $\pm 6$ -ms time resolution of the hodoscope data. These sites (decreased counting rate) are shown by open circles in Fig. 49. Sites showing an increase in counting rate at 29.77 s are shown by solid diamonds. The size of the symbol is a rough indication of the initial rate of change at this time. Only the initial direction of change was considered; e.g., in Rows 7-11 of column 9, the initial increase lasted no more than 30 ms before reversing.

The upward velocity of the top of the fuel cannot be calculated, since there was only one row of hodoscope detectors completely above the original fuel column. A lower-limit velocity of 30 in./s, however, can be inferred from the slope of the increase in the signal from the detectors in Row 2, which took about 50 ms to complete. We note also that the start of upward motion at the

area of the hodoscope. The 10% loss was estimated from the reduced counting rate, integrated overall scales, and corrected-for background at the time of the eruption.

In addition to the fuel that went up, a little fuel near the midplane moved away from the pump, presumably to the wall of the pressure vessel. Near the bottom, some fuel moved toward the pump.

Figure 47 shows the situation shortly before the eruption. Comparison with Fig. 48 reveals that the regions showing a decrease in fuel content during the eruption were those where the preeruption fuel concentration was highest and where, therefore, the rate of heat generation per unit volume was greatest. This is true even though Fig. 47 shows a net deficit in those regions with respect to the initial configuration; the deficits in the other portions of the original fuel zone (except the top and bottom, where the temperatures and fission rates were somewhat lower) were greater. The increases that Fig. 47 shows outside the original fuel zone represent fuel

top of the fuel was essentially simultaneous with the start of voiding at the center. The same holds for the lateral motions of the fuel.

Figure 50 shows the situation shortly after the eructation, at 30.5 s, with respect to the 8-s configuration. Much of the region originally occupied by the fuel was almost completely voided. Up to this point there was only a relatively small amount of downward motion of the fuel, resulting in some accumulation at the lower part of the side away from the pump.

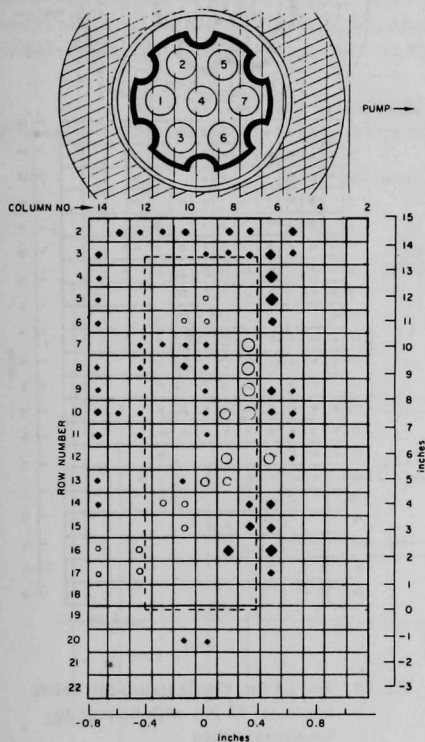


Fig. 49. Initial Fuel Motion Associated with Eructation at 29.77 s. (The open circles represent an initial decrease in counting rate, the solid diamonds an initial increase. The larger the symbol, the greater the rate of change at 29.77 s.)

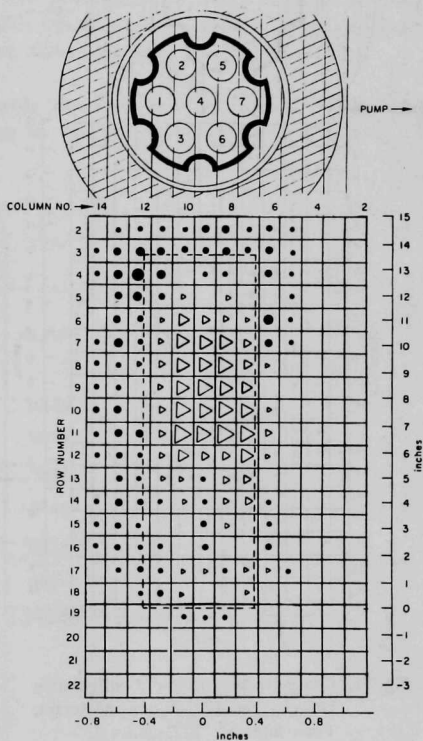


Fig. 50. Test L3 Fuel Configuration at 30.5 s with Respect to 8-s Configuration

Posteructation Period. Shutdown began at 33.9 s. Some fuel motion occurred after the eructation. Figure 51 shows the net change between 31.2 and 33.9 s. Principally, some fuel settled from Rows 4-6 into Rows 7-10, and from Rows 12 and 13 into the region below.

Figure 52 shows the disposition of fuel at shutdown, relative to the 8-s configuration. Some fuel was still moving at shutdown, but the motion was minor, a conclusion that is supported by the fact that Fig. 52 correlates well with the posttest neutron radiographs.

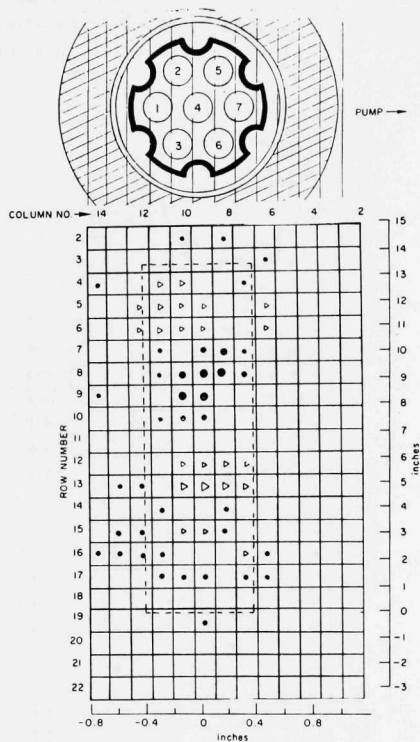


Fig. 51. Change in Test L3 Fuel Configuration between End of Eruption and Scram; Time Interval: 31.2-33.9 s

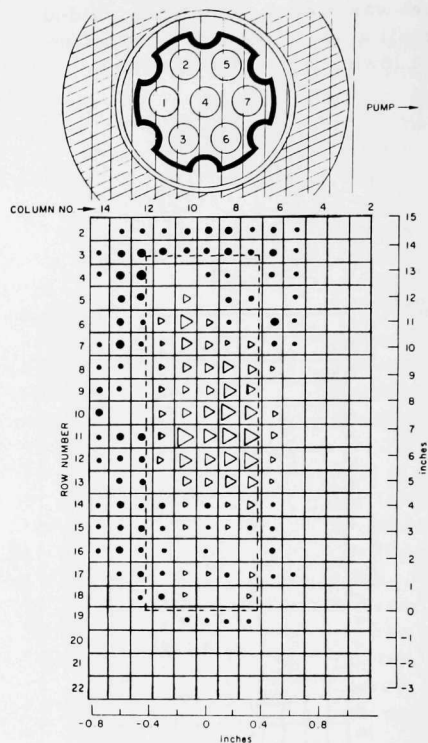


Fig. 52. Test L3 Fuel Configuration Just before Scram (at 33.9 s) with Respect to 8-s Configuration

## D. Results of Posttest Examination

### 1. Disassembly of the Loop

The initial posttest disassembly of the L3 loop was done in the Hot Fuel Examination Facility (HFEF) at ANL-West. The loop was stripped and cut into sections without removing the sodium. The test section, the bottom bend of the loop, the upper bend between the pump and the test section, and the plenum section of the loop with part of the test-section cruciform extension were shipped to the Materials Science Division Alpha Gamma Hot Cell Facility (MSD-AGHCF) at ANL-East for further disassembly and examination.

The part of the loop containing the test section was cut into small pieces with an abrasive wheel according to the scheme shown in Fig. 53. The

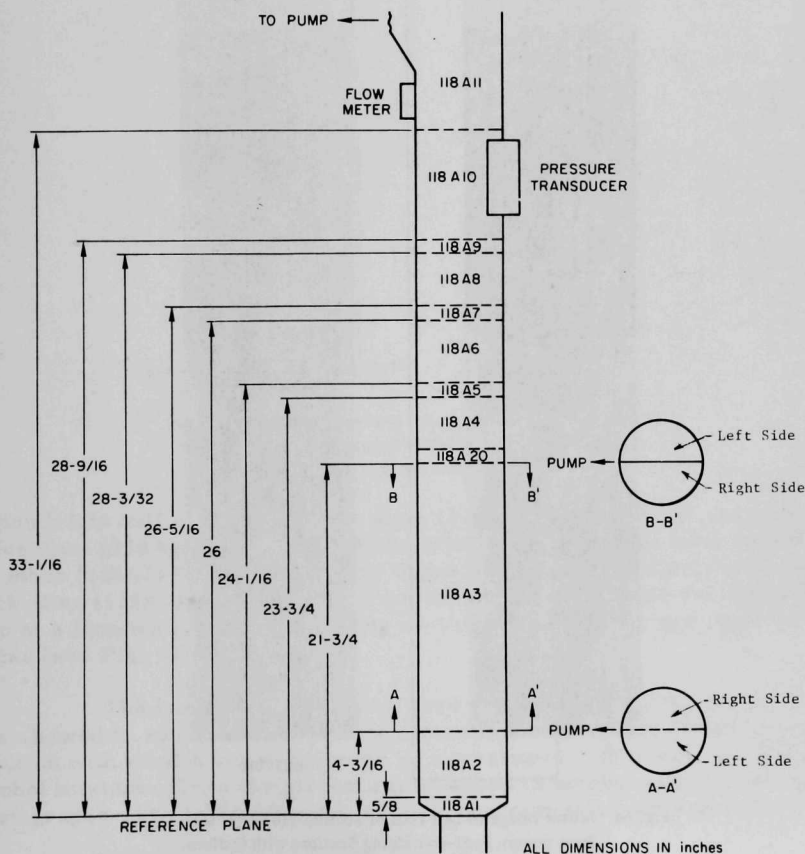


Fig. 53. Sectioning Scheme for Test Section of Test L3

transverse cuts were made first. The resulting long section, which contained the bulk of the fuel-column remains, was subsequently cut longitudinally in a plane passing through the principal axes of the pump and the test section.

The paraffin used to lubricate the cutting wheel tended to fill in the open spaces inside the test section. Therefore, after the various pieces were separated, they were treated with petroleum ether to dissolve the wax. The exposed surfaces were photographed after the wax was removed. Figures 54 and 55 show the exposed surfaces of the long fuel-containing section after cutting axially and with the sodium in place.

Three 1/2-in.-thick transverse slices were cut from one of the long, semicircular sections obtained by the lengthwise cut through the fuel

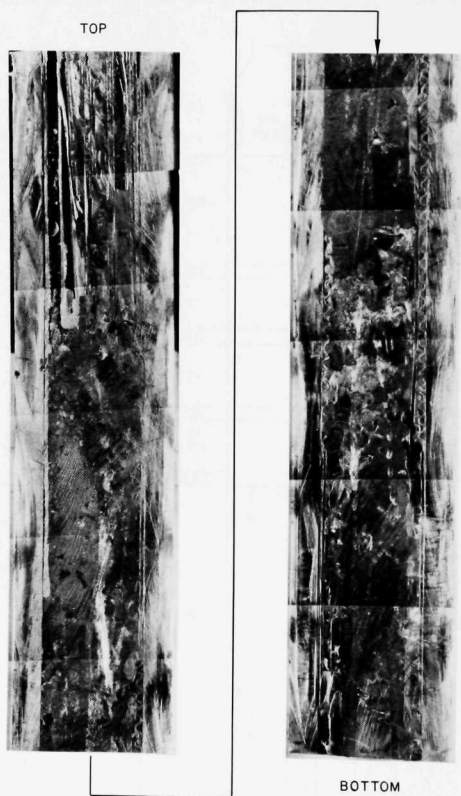


Fig. 54. Mirror Image of Left Half of Section 118A3 (as seen from pump); Fuel-containing Sections with Sodium. Mag.  $\sim 0.6X$ . Neg. No. MSD-169061.

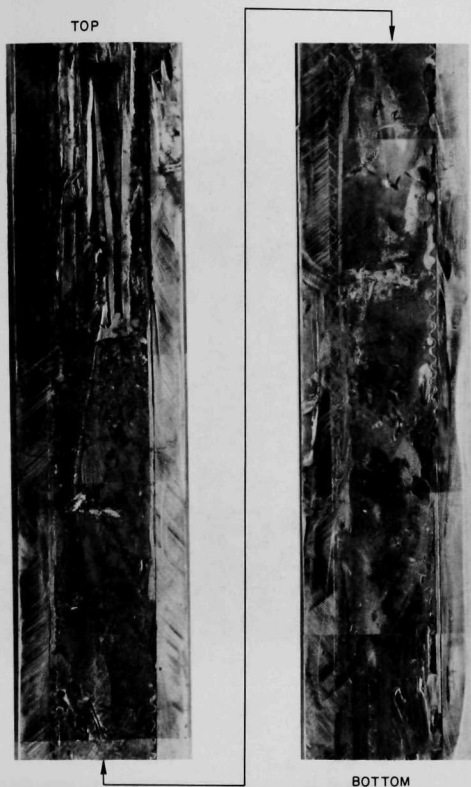
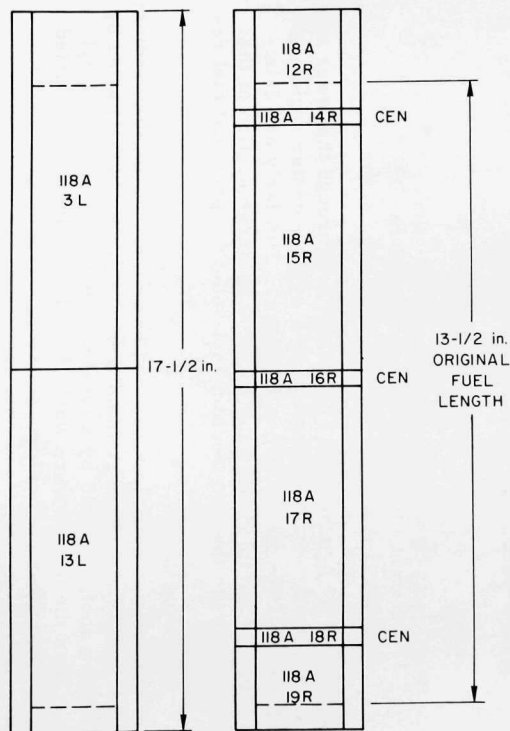


Fig. 55. Mirror Image of Right Half of Section 118A3 (as seen from pump); Fuel-containing Sections with Sodium. Mag.  $\sim 0.6X$ . Neg. No. MSD-169062.

region (right half of Fig. 56). One slice (118A18R) was through the lower mass of fuel, one (118A16R) was through the relatively fuel-free center region, and the other (118A14R) was through the upper fuel mass. Similarly a 1/2-in.-thick slice (118A20) was obtained from the entire transverse section of the loop at a location just above the long section containing the principal fuel remains (see Fig. 53).

The various other pieces were then heated, and the melted sodium was allowed to run out. The sodium remaining on the pieces was removed by reaction with ethyl alcohol, followed by a treatment with a water-50% ethyl alcohol mixture. Then the pieces were washed in alcohol and vacuum-dried. Photographs were taken after the sodium was removed (see Figs. 57-61).



L and R indicate left and right longitudinal sections as seen from pump.

Fig. 56. Samples Initially Cut from Fuel-containing Part at Test Section

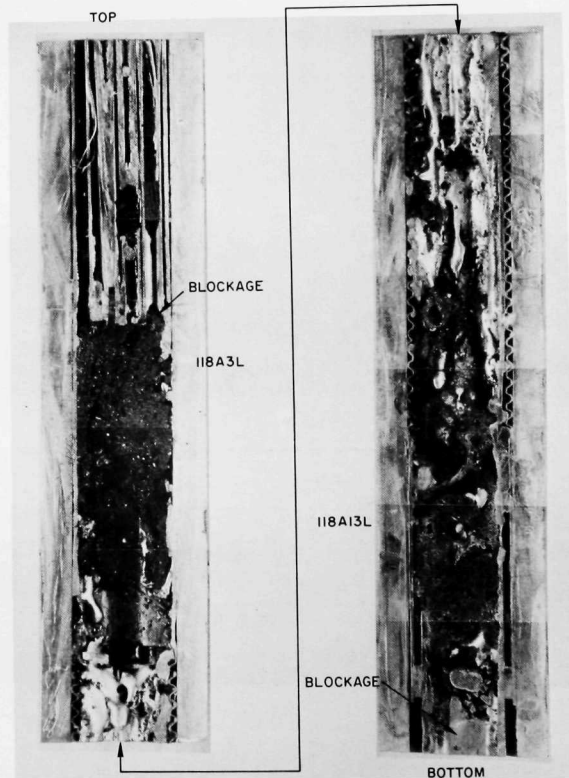


Fig. 57. Mirror Images of Sections 118A3L and 118A13L after Sodium Removal, Showing Blockages at Bottom of Elements at Lower Right and above Fuel Mass at Upper Left. Mag. ~0.6X. Neg. No. MSD-168948.



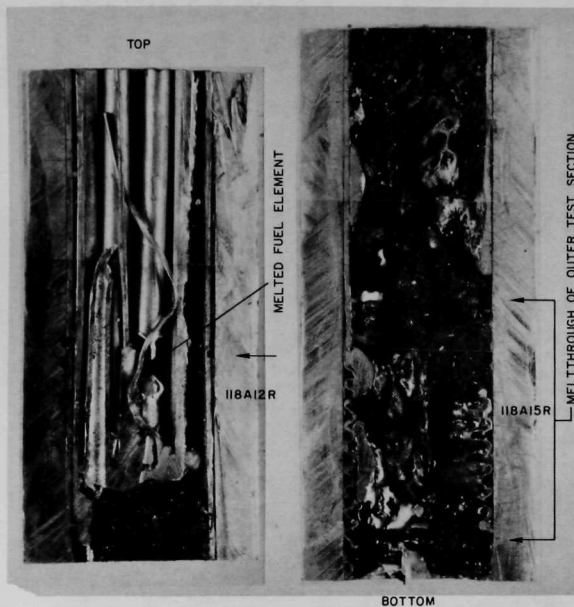


Fig. 58. Mirror Images of Sections 118A12R and 118A15R after Sodium Removal, Showing Melting of Elements 17-15 above Fuel Column and Meltthrough of Outer Test-section Tube. Mag.  $\sim 0.9X$ . Neg. No. MSD-169066.

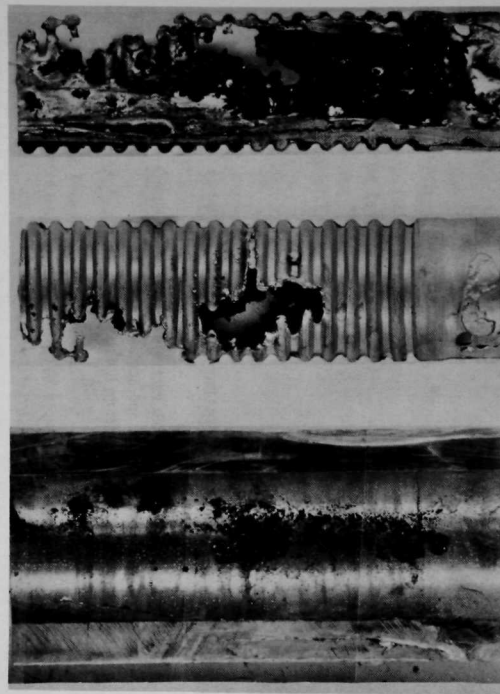


Fig. 59. Mirror Images of Section 118A17R after Sodium Removal, Showing Front and Back Views of Bellows and Inside of Loop Wall at Mid-length of Original Fuel Region. Mag.  $\sim 0.9X$ . Neg. No. MSD-169063.

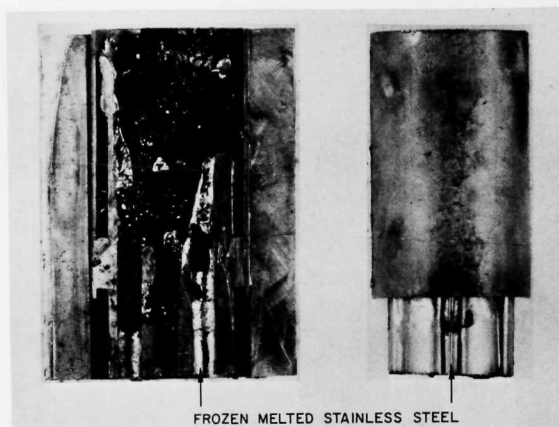


Fig. 60. Mirror Image of Section 118A19R after Sodium Removal, Showing Bottom Blockage (left) and Backside of Test-section Tube after Separation from Loop Wall. Mag.  $\sim 0.9X$ . Neg. No. MSD-169065.



Fig. 61

Mirror Image of Bottom End Plug after Sodium Removal. Mag.  $\sim 0.9X$ . Neg. No. MSD-168218.

The sodium removed by heating was reacted with ethyl alcohol, and the insoluble residue from each section was separately collected. Residues resulting from the alcohol dissolution of the sodium remaining in the sections were also separately collected from each piece. These residues were examined as described later.

Some of the sections tended to come apart after the sodium was removed (see Figs. 59 and 60). Consequently, the fuel-containing sections were filled with epoxy to help hold the various components in place. Several specimen were cut from the epoxy-filled sections for macro-examination of the remains of the fuel elements and, in some cases, for detailed microscopic examination of the structures.

The bottom bend of the loop was cut into smaller sections, and the sodium was removed to recover and examine the neutron-absorbing material observed in this location on the neutron radiographs.

## 2. General Observations

According to the neutron radiograph of the stripped L3 loop, about a 3-in.-long mass of high-density neutron-absorbing material, presumably fuel, was present toward the bottom of the fuel-column region. Below this mass of fuel, scattered indications of neutron-absorbing material could be seen among the end plugs and in the region of the 1/2-in. length of insulator pellets.

Above the bottom mass of fuel, for about 8 in., the neutron-absorbing material was less dense and more scattered, with the lesser quantity on the side of the loop toward the pump. Above this region, about 2.5 in. of high-density neutron-absorbing material was present.

On the neutron radiograph, above the original top of the fuel column, scattered neutron-absorbing material of varying density was visible for ~2.5 in. Random indications of fuel material were found for an additional 7.5 in. upward. The topmost indications appeared as a curving pattern.

In the opened test section, sodium occupied the space not occupied by fuel or steel from the bottom of the elements up to the top of the fuel column, but not up to the top of the pins. A few small voids were present in the sodium, as seen in Figs. 54 and 55. Below the bottom end plugs, at the juncture between the test section and the smaller tube from the pump, there was an appreciable void in the sodium, apparently due to shrinkage on cooling. Above the top of the fuel columns, the space around the plenums of the elements contained only a small amount of sodium. A plug of sodium did seem to be present at the tops of the elements. Considerable void space existed below the top crust of sodium. This space is believed to result from shrinkage of the sodium as it filled the available space in the fuel region of the test section. Sodium did not appear to have moved through the region around the bottom of the elements during cooling.

After the sodium was removed from the test-section pieces, warping was seen in the remains of the fluted tube. In Figs. 54 and 55, one can see that the top of the fluted tube shifted away from the pump. In Fig. 57, for section 118A13L, the fluted tube has a bend when it still exists alongside the bellows.

The observed distribution of fuel conformed to the distribution of neutron-absorbing material observed in the posttest neutron radiograph.

### 3. Fuel-column Region

a. Blockage at Bottom. The blockage at the bottom of the fuel elements appeared to be complete. It consisted of melted stainless steel around the elements in the vicinity of the insulator pellets for a distance about two fuel pellets long above the insulator pellets as shown in sections 118A13L and 118A19R (see Figs. 57 and 60, respectively). Other views of this blockage are shown in Figs. 62-64. Fuel in the region about three pellets high above the bottom two fuel pellets was cracked, but did not appear to have melted. Some large globules of metal were also found in this region. The broken-fuel-pellet region merged into a region about 2 in. long farther up, consisting of porous melted fuel.

Below the insulator pellets, the stainless steel blockage did not fill in completely around the bottom end plugs of the fuel elements (see Fig. 61). Two bottom-end plugs (of PNL-17-8 and -40) were loosened from the others. The other five were held together by the stainless steel solidified around them. Fusion between the end plugs and the melted steel was not observed.

b. Blockage at Top. The blockage just above the tops of the original fuel pins appeared to possibly have several channels through it. This possibility is supported by the fact that there was little sodium around the plenums of the elements and much sodium in the fuel section.

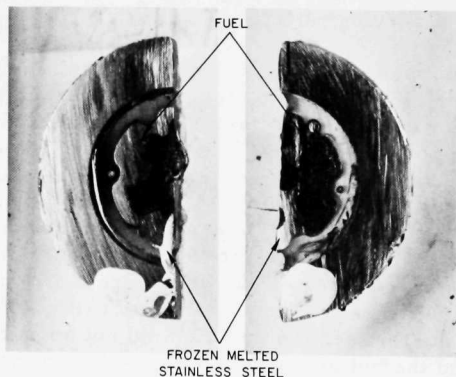


Fig. 62

Mirror Images of Transverse Sections from Vicinity of Bottom Blockage below Header. Mag. ~1X. Neg. Nos. MSD-166882 and -166883.

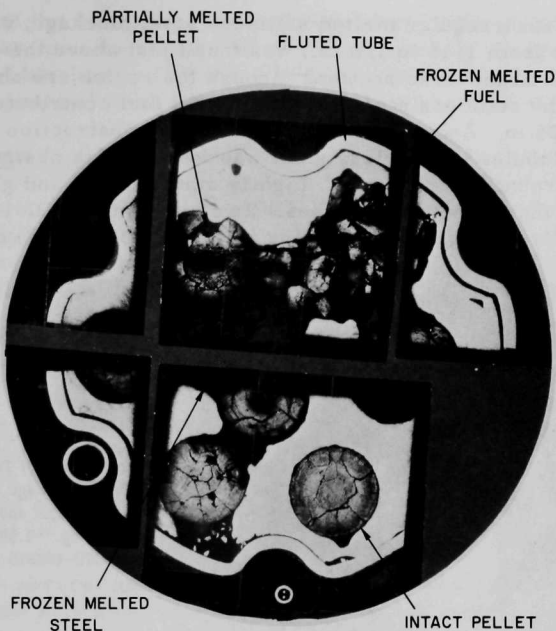
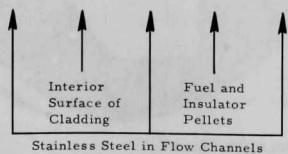


Fig. 63. Composite of Transverse Sections through Bottom Blockage, Showing Distribution of Fuel and Melted Stainless Steel. Mag.  $\sim 3.25X$ . Neg. No. 169143.



Fig. 64

Bottom of Fuel Column, Showing Stainless Steel Blockage; Section 118A19R. Mag.  $\sim 2.75X$ . Neg. No. MSD-169067.



An irregular melted stainless steel blockage, varying in apparent thickness from  $1/16$  to  $1/2$  in., was found just above the original top of the fuel column. Transverse sections through the region are shown in Figs. 65 and 66. Below the stainless steel, porous melted fuel contributed to the blockage for about 1.25 in. Above the stainless steel, an obstruction of lightly sintered fuel and globules of stainless steel was found. This obstruction did not fill the spaces around the elements. Lightly sintered fuel and globules of metal were also found inside the spacer tubes. Two elements, PNL-17-31 and -15, had melted locally through their cladding (see Figs. 57 and 58) above the

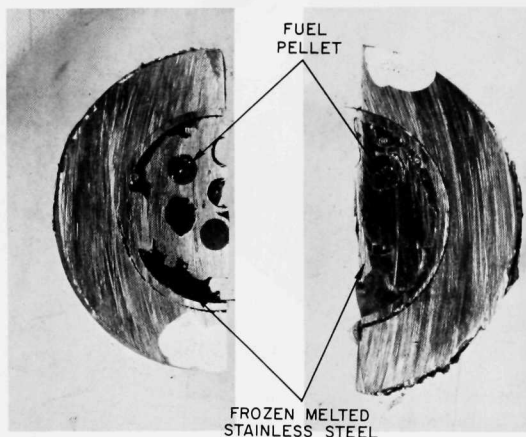
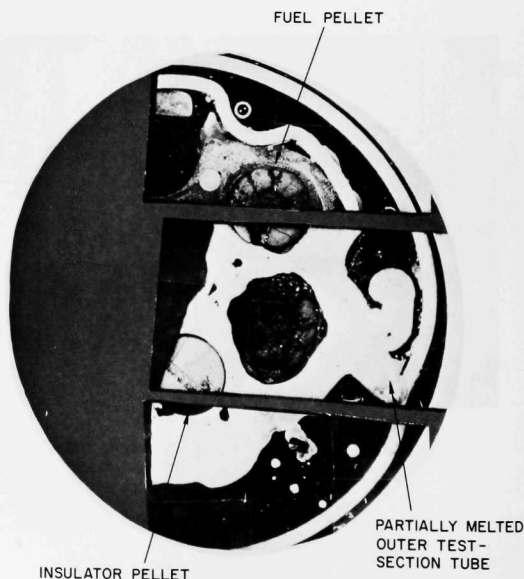


Fig. 65

Mirror Images of Transverse Sections at Upper Blockage, Showing Relationship of Pellets and Melted Stainless Steel. Mag.  $\sim 1.25X$ . Neg. Nos. MSD-166876 and -166879.

Fig. 66

Composite of Transverse Section at Upper Blockage, Showing Partial Melting of Outer Test-section Tube. Mag.  $\sim 3X$ . As polished. Neg. No. MSD-169141.



original tops of the fuel pins. The meltthrough appeared to have left voids in the elements at these locations and may have provided channels through the stainless steel blockage. The space between the fluted tube and the outer test-section tube appeared to be relatively free of debris down to the fuel plug.

#### 4. Extent of Melting

Evidence for melting of the loop tube along the test section was not observed. Direct evidence for fusion of the outer test-section tube to the loop wall was not seen, but the fact that much of the test section was stuck in the loop implied that local fusion had occurred.

The outer test-section tube appeared to be intact above where it joined the bellows, except for two places. The bellows sections of the outer tube extended along the middle 6 in. of the original fuel columns. Near the upper stainless steel blockage the outer tube had melted (see Fig. 66), but had not flowed away. Just above where it joined the bellows, the outer tube had melted through on the side away from the pump (see Figs. 57 and 58). Steel that had melted and resolidified was in close contact with the inside of this tube at several locations along its length.

In several places the bellows was locally melted, and more melting occurred on the side away from the pump, as indicated in the mirror-image photograph of section 118A17R in Fig. 59. Melted steel adhered to the inside of the bellows at several locations. The fuel that had gone through the opening in the bellows in section 118A17R was lightly sintered to the loop wall.

Greater melting of the bellows on the side away from the pump is consistent with the hodoscope results in the 22-26-s period. The hodoscope showed that, by 23.5 s, fuel motion away from the pump had occurred in the upper two-thirds of the fuel column. At 26 s, according to Fig. 46, fuel had moved away from the pump to the upper, middle, and, to a lesser extent, the lower regions. Fuel that was found in the posttest examination to be once molten and/or sintered to the loop wall was not necessarily molten when it moved through the fluted tube or the bellows. It may have been hot enough to melt the steel without being molten itself, but melted after it had made its penetrations. In Sec. IV.C it was pointed out that the data were consistent with the motion of whole pellets.

The lower part of the outer test-section tube below the bellows was generally intact all the way to the heater, but melted steel adhered to many places on the inside.

The fluted tube was intact down to the upper blockage. Over the length of the fuel column, most of the fluted tube had melted away, but remnants of it seemed somewhat more persistent along the fuel pins on the side toward the pump. At the bottom, this fluted tube was intact up to the bottom header.

In the vicinity of the header, it was intact for about 1 in. above the header on the side toward the pump and about 3/8 in. above the header on the opposite side (see Fig. 60).

Above the upper blockage, the cladding and spacer wires were intact, except for the local burn-through on elements PNL-17-31 and -15. Near the stainless steel blockage at the top, cladding remains were visible for elements PNL-17-22 and -40, and most of the spacer wires could be seen. Elsewhere along the length of the fuel pins, cladding or spacer wires were not evident until below the bottom header. Spacer wires became evident first, with cladding visible, in the vicinity of the bottom fuel pellet.

Fuel pellets were in evidence only at and above the top of the original fuel column, and at the bottom of the fuel column. At the bottom of the fuel region, columns of fuel four to six pellets high were observed in a cracked and perhaps partially melted condition. A large mass of melted fuel was present at both the top and bottom of the fuel column, as seen in Figs. 57, 58, and 60. Only a relatively small amount of melted fuel was within the bellows region, where it tended to cling in pockets on the melted steel along the wall.

Neither melted fuel nor melted steel had moved as far downward at the bottom of the L3 cluster as in Test L2.

#### 5. Evidence for Flows of Molten Stainless Steel

In Test L2, evidence for two separate flows of melted stainless steel was observed near the bottoms of the fuel column. The evidence consisted of a fine-grained "chill-cast" layer of one flow of melted steel against another. Similar evidence was not observed for Test L3.

However, a transverse slice through the tops of the bottom end plugs of the elements (see Fig. 67) showed two principal areas of melted stainless steel that had frozen among the end plugs. One area appeared to be all stainless steel with a cast dendritic structure as shown in Fig. 68. The other area also had a structure, but it included several particles of once-melted fuel, as shown in Fig. 68. The difference in structure between the two patches of steel may be indicative of slower cooling of the steel containing the fuel particles. The steel containing the fuel particles probably came down and solidified later than the other region of solidified steel.

Detailed examination of the distribution and flow patterns of melted stainless steel was inconclusive in providing other evidence for more than one flow of stainless steel.

#### 6. Morphology of the Fuel

The relationship between melted fuel and melted stainless steel appeared to be the same in Test L3 as in Test L2. Globules of metal, assumed



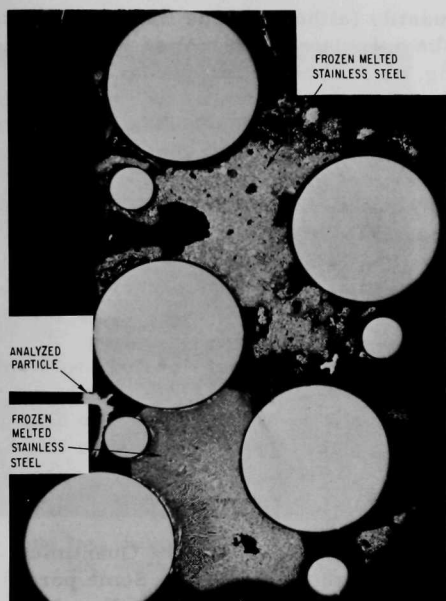
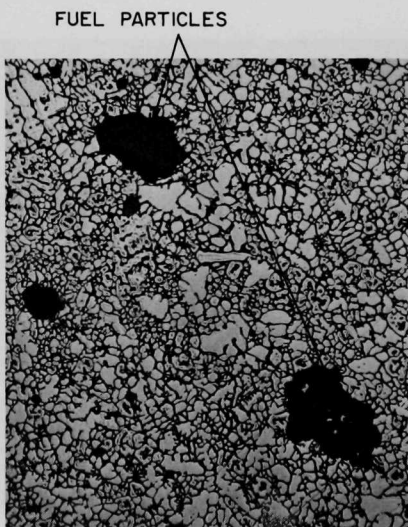


Fig. 67

Transverse Section through Top of Bottom End Plugs, Showing Two Types of Melted Material. Mag.  $\sim 5.5X$ . Neg. No. MSD-169064.



(a) No Fuel



(b) Fuel Particles Present

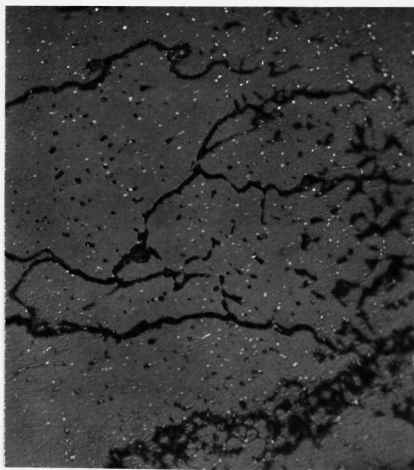
Fig. 68. Cast Steel Structure at Two Locations Next to Bottom End Plugs. Mag.  $\sim 85X$ . Etched. Neg. Nos. MSD-168534 and -168535.

to be stainless steel because of the quantity (although some fission products could be included), were observed to be associated with melted fuel in various degrees of dispersion, as shown in Fig. 69. Globules of metal as small as  $\sim 1 \mu\text{m}$  (see Fig. 69) were partly dispersed on grain boundaries. Other globules varied in size up to relatively large masses among the grains of fuel (see Fig. 69). As measured with a Quantimet Analyzer, a series of 15 measurements on areas containing a fine dispersion of globules gave  $2.5 \pm 1.3$  areal %. In Test L2, a source of stainless steel globules in melted fuel was observed at one specific location. A similar situation was not seen on any of the L3 specimens examined. Some areas of melted fuel appeared to be free of metallic particles (see Fig. 70). One or two small intrusions of melted metal into unmelted fuel were observed, as shown in Fig. 71.

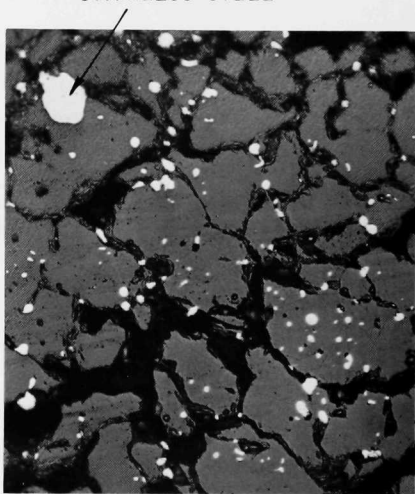
The gains of melted fuel commonly had dimensions of  $38\text{--}56 \mu\text{m}$ , about 5 to 10 times as large as the grains in the original pellets. Some of the grains in the irradiated unmelted fuel pellets were about as large as shown in Fig. 72. Elongated grains of melted fuel also were found, as seen in Fig. 69c. A wide variation of grain size could occur in a local area (see Fig. 73).

Porosity in bulk melted fuel, as measured with the Quantimet Analyzer, ranged from 28 to 42 areal % in 15 measurements. Some pores within a grain (see Fig. 74) measured 7 areal % of the grain. In Fig. 74b,

#### STAINLESS STEEL



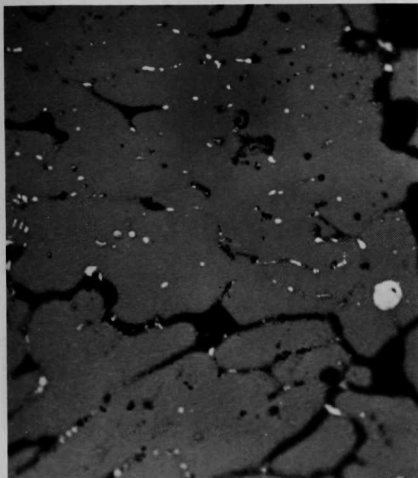
(a) From Lower Mass of Fuel. Mag.  $\sim 430\times$ .  
Etched. Neg. No. MSD-167784.



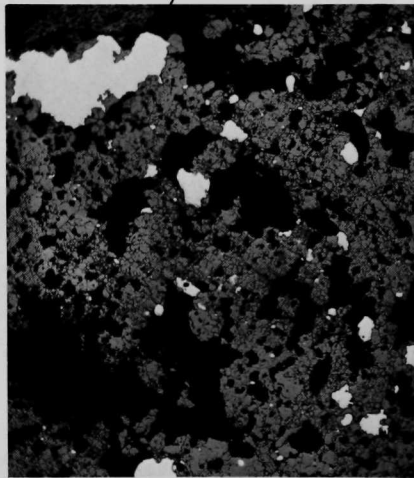
(b) From Upper Mass of Fuel. Mag.  $\sim 430\times$ .  
Etched. Neg. No. MSD-166972.

Fig. 69. Dispersion of Stainless Steel Globules in Melted Fuel

STAINLESS STEEL



(c) From Midlength of Fuel Column.  
Mag.  $\sim 430X$ . Neg. No. MSD-167097.



(d) From Upper Mass of Fuel. Mag.  $\sim 43X$ .  
Neg. No. MSD-167866.

Fig. 69 (Contd.)

STAINLESS STEEL

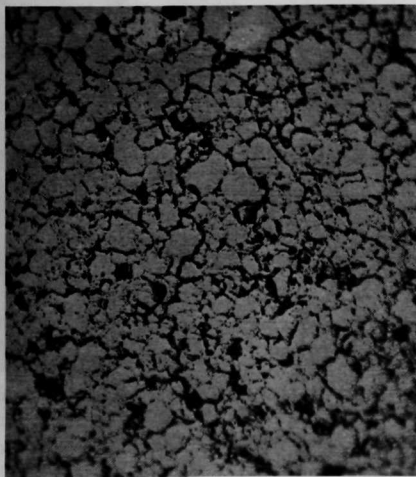


Fig. 70. Melted Fuel with No Metallic Particles  
from Approximate Midlength of Orig-  
inal Fuel Column. Mag.  $\sim 430X$ .  
Etched. Neg. No. MSD-167039.

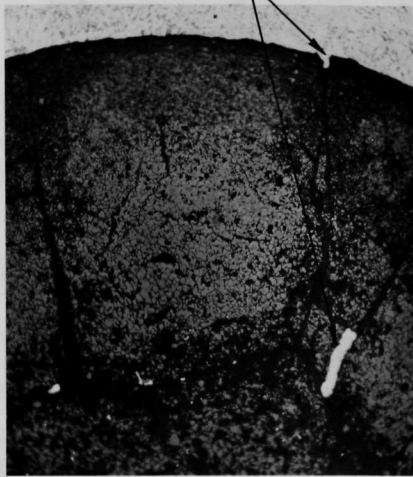


Fig. 71. Intrusion of Metal into Unmelted Fuel at  
Top of Fuel Column. Mag.  $\sim 43X$ .  
Etched. Neg. No. MSD-168280.

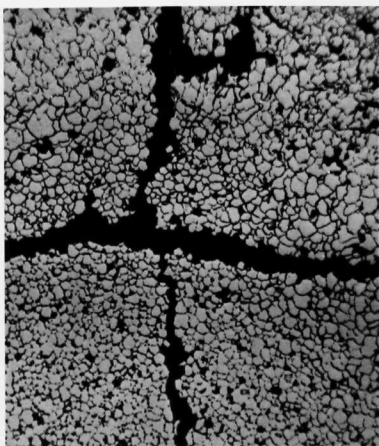


Fig. 72. Cracked, Unmelted Fuel from Bottom Pellet. Mag.  $\sim 80\times$ . Etched. Neg. No. MSD-167079.

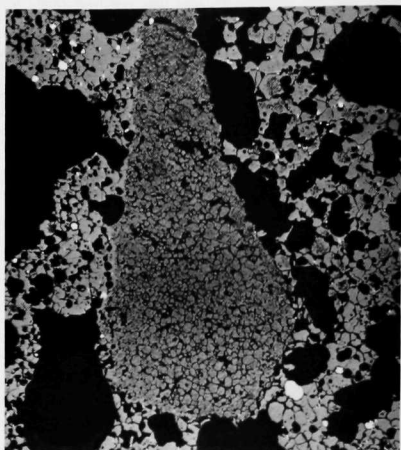
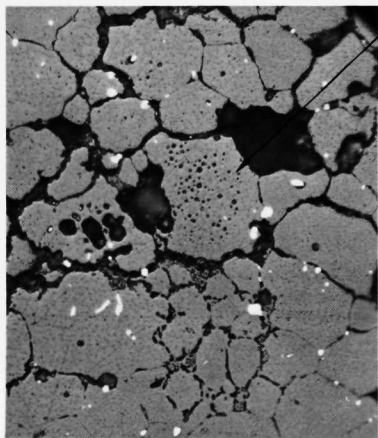
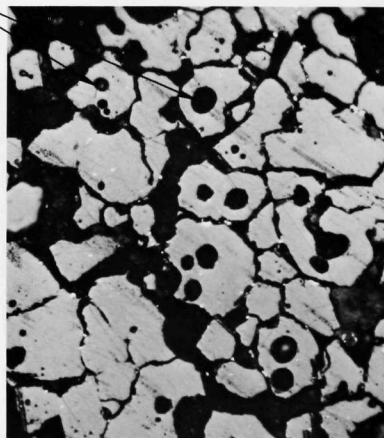


Fig. 73. Grain-size Variation in Upper Fuel Mass. Mag.  $\sim 70\times$ . Etched. Neg. No. MSD-167875.

#### POROSITY



(a) Porosity within Grains



(b) Consolidation of Fine Porosity within Grains

Fig. 74. Porosity within Grains of Melted Fuel at Top of Upper Mass of Fuel. Mag.  $\sim 400\times$ . Etched. Neg. Nos. MSD-167868 and - 167021.

consolidation of fine porosity within grains appears to have occurred. The unmelted fuel in Fig. 72 had 16 areal % porosity, exclusive of the crack.

One particle of fuel in the bellows section had a large internal void and thin walls, fitting the description of froth (see Fig. 75). This type of fuel particles was rarely observed.

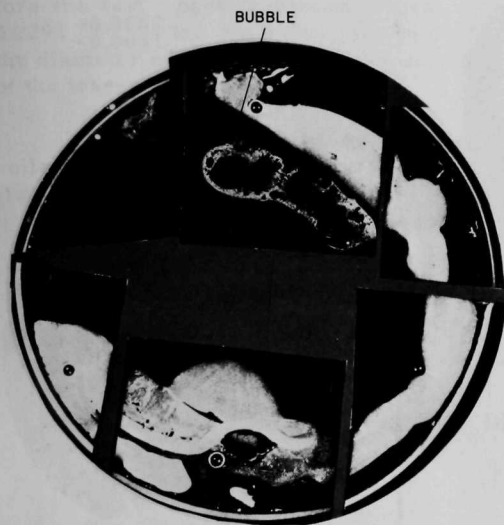


Fig. 75

Composite of Transverse Section near Original Midplane of Fuel Column with Large Frothlike Bubble of Fuel. Mag.  $\sim 3X$ . Neg. No. MSD-169145.

## 7. Plenum Region of Fuel Elements

The neutron radiographs of the test section after the transient had shown curving patterns of neutron-absorbing material in the region of the plenums, along with other indications of neutron absorption. The cutting scheme of Fig. 53 was designed to help investigate these items.

The curving neutron-absorption pattern was found to be due to a small amount of fuel trapped against a thermocouple that spiraled down between the fluted tube and the outer test-section tube (see Fig. 76). The other indications were due to particles of fuel both around the plenums of the fuel elements and inside the plenums. Small globules of metal, presumably stainless steel, were also observed in this region. One large pellet of metal was removed from a spacer tube from section 118A4 and is shown in Fig. 77.

About 3 in. of the top ends of the fuel elements were in section 118A10 (see Fig. 53). Length measurements were made of the top part of each element. The results for the seven elements were  $3.12^{+0.10}_{-0.08}$  in. These results confirm the radiograph evidence that the relative axial displacement among the elements was small. No evidence was found to indicate that the tops of the fuel pins might have moved up or down as a unit.

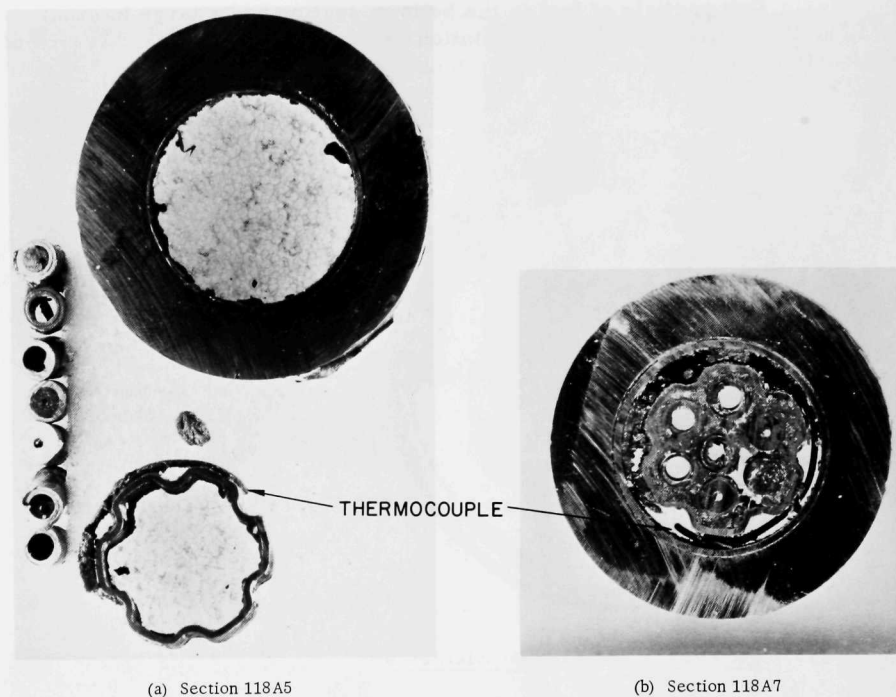


Fig. 76. Fuel Deposited on a Thermocouple between Outer Tube and Inner Fluted Tube. Mag.  $\sim 1.3X$ . Neg. Nos. MSD-166334 and -166339.

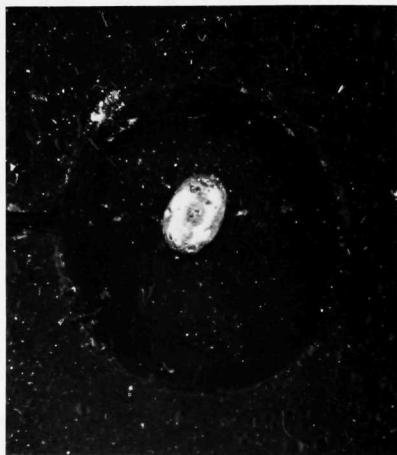


Fig. 77  
Metallic Ingot Recovered from Spacer  
Tube; Section 118A4. Mag.  $\sim 2.4X$ .  
Neg. No. MSD-166919.

Numerous diameter measurements, perpendicular to each other, were made on the plenums of the pins. These data may be compared with diameters measured in corresponding locations on the irradiated elements before the test: postirradiation pretest,  $0.2292^{+0.0006}_{-0.0009}$  in.; posttest,  $0.2291^{+0.0067}_{-0.0011}$  in. No indications of ovality were found, and we conclude that the diameter of the cladding in the plenum region was not altered as a result of the loss-of-flow test.

The plenum sections at the top of the fuel elements contained a coiled spring above a tubular spacer. X radiographs of the elements after irradiation in EBR-II had shown that the springs and the spacers were in their original positions. The springs appeared to be slightly shorter than the original 6-in. reference length. Measurements from the radiographs indicated that the number of coils per inch at the bottom of the springs was one or two coils more than at the top.

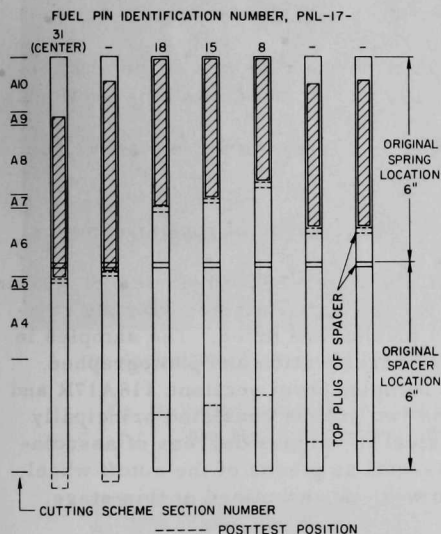


Fig. 78. Relative Pre- and Posttest Locations of Spring and Spacer in Plenums of Fuel Pins

Observations on the parts of the springs and spacer tubes recovered from the plenums of the pins made possible a reconstruction of the physical relationship between the springs, the spacer tubes, and the tops of the pins. The position of the plugs at the top of the spacer tubes as seen in photographs was used in reconstructing the relationship shown in Fig. 78. Four of the plenum sections could be identified by position in the test section with respect to the pump, but the other three could not.

The lengths of the springs were estimated from the lengths of the parts after making allowance for the cuts. The coils per half-inch of spring were counted at both ends of the springs with

the following results: top, 17-20 coils/in.; bottom, 28-36 coils/in. Since the spring wire was 0.025 in. in diameter, the completely compressed spring would have 40 coils/in. In some cases, the spring was almost completely relaxed toward the bottom while the top retained essentially the original coil spacing, indicating that a temperature differential had been imposed during a compressive stress on the springs.

Two spacer tubes appear to have dropped to a position below their original position by a small amount, as shown in Fig. 78. The other spacer tubes had moved upward. The region where the insulator pellets of  $\text{UO}_2$  abutted



the open bottom of the spacer tube changed appreciably. An upward movement of fuel appears to have crushed the insulator pellets and pushed the resulting debris up into the spacer tubes in some of the elements (see Figs. 57 and 58). Some fuel was also ejected up into the spacer tubes. In two locations, the cladding was melted through above the original top of the fuel column (elements PNL-17-31 and -15), apparently by hot, displaced fuel.

## 8. Powders

Powders were obtained from various locations, as described in Sec. IV.D.1.

- a. Six samples were recovered from the sodium melted out of the fuel-containing sections of the test section.
- b. Six samples were obtained from the residues of the alcohol treatment to remove the remaining sodium from the fuel-containing sections.
- c. Eleven samples were recovered from the sodium above and below the sections containing most of the fuel.

Only a limited amount of work was done on these groups of powder samples.

All powders were treated with a water-50% ethyl alcohol mixture to dissolve any sodium alcoholate; the solutions were decanted, and the residues were rinsed (by decantation) in ethyl alcohol and dried. The samples in the first two groups were examined at low magnification and photographed. Figure 79 shows typical appearances for samples from sections 118A17R and 118A3L (see Fig. 56). The material in the two groups consisted principally of particles of melted fuel and stainless steel in various degrees of association. One or two pieces of fuel pellets, as well as pieces of the cutoff wheel, were also found. The samples in group c were not examined at this stage, but in the next one to be described.

Except for one sample from group c, all samples in the three groups were treated with methylene iodide (density of  $3.325 \text{ g/cm}^3$  at  $20^\circ\text{C}$ ) to float off light debris that was principally introduced during handling. These specimens were then washed in alcohol and dried. The sample from group c that was exempted from the above treatment was collected from the bottom bend of the loop and weighed 1.28 g. It comprised fuel, stainless steel, and a small piece of a thermocouple. This latter sample was only cleaned of sodium alcoholate, examined at low magnification, and photographed (see Fig. 80). It appeared to be chiefly globules and spatters of stainless steel with some pieces of fuel. This material has been noted on the neutron radiograph.

Immersion densities in carbon tetrachloride were determined for the six samples in group b and for two samples in group a; the results are

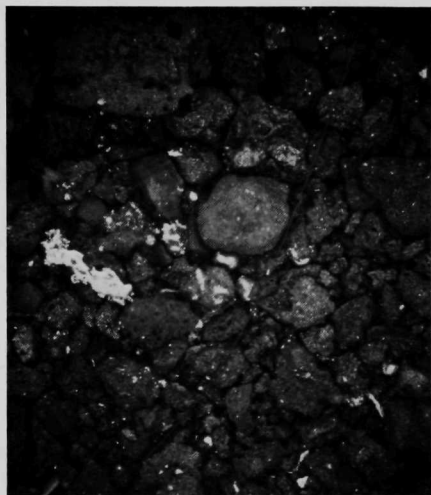


given in Table III. The samples in group c, except the sample from the bottom bend, were weighed after flotation; Table IV gives the results as grams of powder per inch of length of the respective portion of the test section.

The dry bulk density was measured for the largest sample in group e with the result  $5.77^{+0.04}_{-0.07}$  g/cm<sup>3</sup>.



(a) Section 118A17R. Mag. ~2.9X.



(b) Section 118A3L. Mag. ~5.5X.

Fig. 79. Particulate Material from Fuel Sections of Loop. Mostly fuel with some stainless steel, and ceramic insulator material. Neg. Nos. MSD-167120 and -167187.

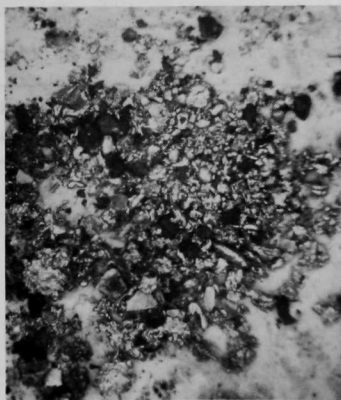


Fig. 80

Powder Sample from Lower Bend of Loop. Mostly stainless steel with some fuel. Mag. ~2.5X. Neg. No. MSD-168159.

TABLE III. Weights and Densities of Powders  
Recovered from Test L3

A. Particles collected from the sodium melted out			
Section Label	Weight as Collected, g	Weight after Flotation, g	Immersion Density, g/cm <sup>3</sup>
118A3L	8.578	7.378	9.62
13L	4.497		
12R	0.606		
15R	2.943		
17R	5.410	5.056	9.21
19R	0.154		
B. Particles collected after reaction of sodium with alcohol			
118A3L	20.075	19.465	9.99
13L	9.684	8.358	9.96
12R	3.697	3.418	9.75
15R	5.561	5.378	9.16
17R	10.982	10.573	9.21
19R	8.051	7.826	9.93
C. Particles from B fractionated by sieving			
Section Label	Sieve Sizes	Weight, g	Immersion Density, g/cm <sup>3</sup>
118A3L	-25/+50	3.879	10.00
	-140/+325	3.522	10.41
	-400	2.202	10.31

TABLE IV. Distribution of Powders along Length of Test Section

Section	Weight Recovered, g	Length of Section, in.	Distributed Weight, g/in.
118A1	0.156	1	0.16
2	0.305	3½	0.09
4	0.487	2	0.24
5	0.626	1/2	1.25
6	0.022	1⅞	0.01
7	1.046	1/2	2.09
8	0.327	1¾	0.19
9	0.124	1/2	0.25
10	0.335	4½	0.08
11	0.002	~14	-

One sample from group a and one from group b were passed through a series of sieves, and the various size fractions were weighed. The results are tabulated in Table V and plotted in Fig. 81. Three of the size fractions from one of the sieved samples were checked for density by the immersion technique, with the results given in Table III.

TABLE V. Particle-size Distribution in Powders  
Recovered from Sections 3L and 17R

Size, $\mu\text{m}$	Section 3L		Section 17R	
	Weight, g	% Cumulative	Weight, g	% Cumulative
<37	2.902	15.5	0.427	8.6
37-44	0.857	20.0	0.087	10.4
44-105	3.522	38.8	0.416	18.8
105-210	2.797	53.7	0.544	29.7
210-297	1.571	62.1	0.377	37.3
297-707	3.879	82.7	1.188	61.3
707-1680	2.277	94.9	0.679	74.9
1680-3360	0.968	100.0	0.468	84.4
>3360	-	-	0.775	100.0
	18.773		4.961	

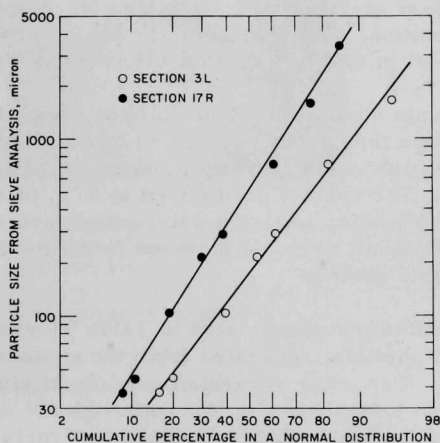


Fig. 81  
Cumulative Size Distribution of Particles

The densities of the collected powders ranged from 9.16 to 9.99 g/cm<sup>3</sup>. The presence of about 35 wt % stainless steel globules and/or closed porosity in the fuel particles could account for the reduced density compared to the theoretical density (11.09 g/cm<sup>3</sup>) and the original average pellet density of 10.31 g/cm<sup>3</sup>. The finer powders that were separated in the sieving appear to be more dense than the coarser powders. The higher density may reflect either less porosity or a lower concentration of steel in the smaller particles.

No further work is planned, and all samples have been stored.

## 9. Microprobe Examination of Samples

Six mounted sections from Test L3 were examined with the MAC450 shielded microprobe to obtain information concerning the distribution of metal, fuel, and urania insulators after the loss-of-flow test in TREAT. Types 316 and 304 stainless steels were differentiated primarily by observing the  $L_{\alpha}$  X-ray line from molybdenum that was present at 2-3% in the former but not in the latter. Fuel ( $UO_2$ -25 wt %  $PuO_2$ ) and urania insulators were determined by using the uranium  $M_{\alpha}$  and plutonium  $M_{\beta}$  X-ray lines.

Two of the most interesting sections were difficult to observe due to problems with polishing materials exuding from cracks and specimen-charging effects. Quantitative results were further complicated by significant alloying of some stainless steel particles with fission-product elements. Ruthenium, technetium, and more molybdenum than expected in Type 316 stainless steel were observed in these particles.

Qualitative and quantitative results are reported for the mounts listed below. The quantitative results were corrected for absorption, fluorescence, atomic number, and deadtime by the MAGIC IV computer program.\*

The stainless steel in mounted section 118A2A was Type 316. Two voids within the largest stainless steel particle contained fragments of fuel of approximately nominal composition. The oxide in the mounted section 118A43 was urania. The stainless steel in mounted section 118A4A was Type 304.

Figure 82 represents mounted section 118A46. Quantitative analysis of the stainless steel in this mount was performed by point-counting for chromium, iron, nickel, and molybdenum. Material balances for these elements ranged from 93 to 97%. The results normalized to 97%, to allow for manganese (2%) and silicon (1%), which were not determined, are shown in Table VI. Ruthenium and technetium were not detected in the melted stainless steel among the end plugs of this section.

The particle of melted metal indicated in Table VI was Type 316 stainless steel. The analyzed particle, separated from the masses of melted metal, is identified in Fig. 82. The other separated particle of similar appearance (labeled as the unanalyzed particle in Fig. 82), although not counted, also appeared to be Type 316 stainless steel. Other fragments of metal were similar to the massive melted metal.

The analyses indicated that the massive melted metal was about two-thirds Type 316 and one-third Type 304 stainless steels. A more accurate

---

\*J. W. Colby, MAGIC IV--A Computer Program for Quantitative Electron Microprobe Analysis, Bell Telephone Laboratory.

deduction of the proportions of the types of stainless steel was not possible since, as shown in the next section, Type 304 stainless steel containing appreciably more nickel than the spacer wires was available for inclusion in the melted steel. Some chromium depletion ( $\sim 15\%$ ) was apparent.

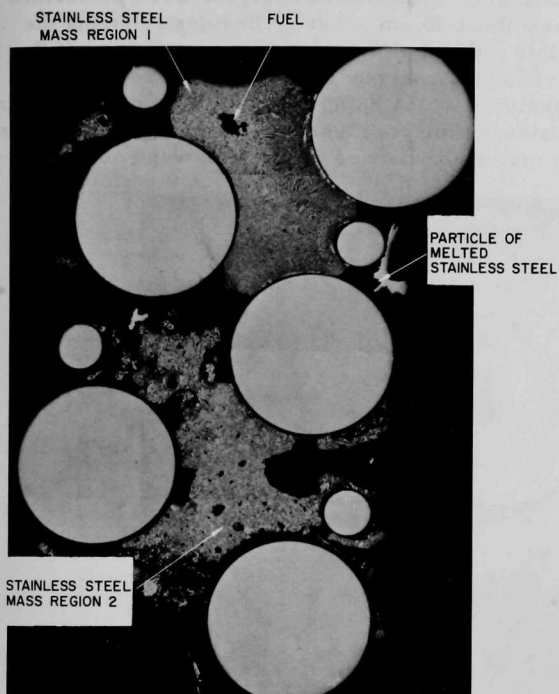


Fig. 82

Section 118A46 through Top of Bottom End Plugs, Showing Composition of Metal and Fuel. Mag.  $\sim 6X$ . Neg. No. MSD-169064.

TABLE VI. Composition<sup>a</sup> of Stainless Steel in Section 118A46

Material	Cr, wt %	Fe, wt %	Ni, wt %	Mo, wt %
Type 316 stainless steel end plugs				
1	16.5	65.4	12.8	2.3
2	16.1	65.9	12.9	2.1
Type 304 stainless steel spacer wires				
1	18.0	70.2	8.7	0.1
2	17.4	71.3	8.3	0.0
Particle of melted stainless steel	16.6	65.4	12.8	2.2
Massive melted stainless steel				
Region 1	15.4	68.3	11.9	1.4
Region 2	15.8	67.1	12.6	1.5

<sup>a</sup>Analyses normalized to 97% to account for manganese (2%) and silicon (1%), which were not determined.

The oxide particles trapped within one (lower mass in Fig. 82) mass of melted steel were fuel of approximately nominal composition.

Figure 83 represents mounted section 118A30R2. Since difficulty was experienced with sample charging, quantitative analyses were performed on this sample by counting areas about 30  $\mu\text{m}$  square. Besides reducing the effects of specimen charging, this method allowed constant monitoring of the sample current image of the area being analyzed. The results are shown in Table VII, the location of the analyzed areas being indicated by a corresponding number in Fig. 83. Material balances for stainless steel were again normalized to 97%. Before normalization, material balances of 95-102% were obtained.

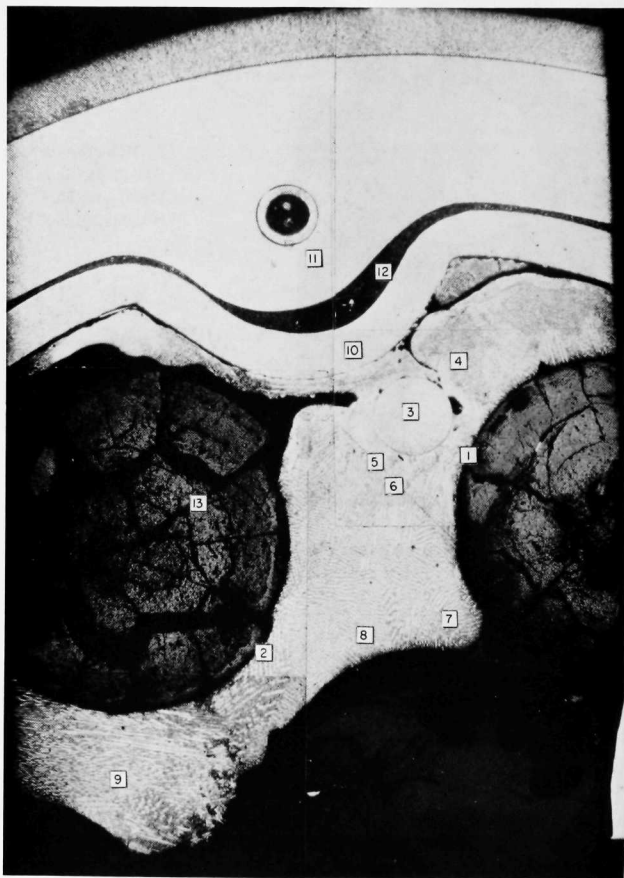


Fig. 83. Section 118A30R2, Showing Locations of Microprobe Analysis. Mag.  $\sim 11\times$ . Neg. No. MSD-181997.

TABLE VII. Composition of Stainless Steel,<sup>a</sup> Nickel Braze, and Metal Particles in Fuel of Section 118A30R2

Material	Cr, %	Fe, %	Ni, %	Mo, %	Ru, %
<u>Cladding Location<sup>a</sup></u>					
1	18.5	66.9	10.7	0.9	
2	17.1	67.1	11.7	1.1	
<u>Spacer Wire<sup>a</sup></u>					
3	18.0	70.4	8.3	0.3	
<u>Melted Steel<sup>a</sup></u>					
4	17.8	67.6	10.9	0.7	
5	17.1	67.4	11.4	1.1	
6	17.0	67.3	11.8	0.9	
7	18.7	65.4	12.1	0.8	
8	16.9	68.3	11.1	0.7	
9	17.8	67.2	11.5	0.5	
<u>Narrow Band<sup>a</sup></u>					
10	18.1	67.7	11.1	0.1	
<u>Wide Band<sup>a</sup></u>					
11	17.7	70.1	9.0	0.2	
<u>Nickel Braze<sup>b</sup></u>					
12	5.9	20.7	69.8	0.1	
<u>Particle in Fuel<sup>b</sup></u>					
13	8.2	53.8	11.9	3.7	1.0

<sup>a</sup>Composition of analyzed elements normalized to 97% to account for manganese (2%) and silicon (1%), which were not determined.

<sup>b</sup>Analyses not normalized.

Also shown are analyses for nickel braze and a particle within a crack of the fuel. These determinations were performed by using a somewhat smaller rastered area than for the stainless steel.

The cladding (Type 316 stainless steel) appears to have melted and thoroughly mixed with the mass of melted steel within this section. Significant visual and analytical differences were not found in these materials.

The source of melted steel was difficult to determine with any certainty. Molybdenum concentrations indicated variable mixtures containing at least half Type 304 stainless steel and the remainder Type 316 stainless steel. Several sources of Type 304 stainless steel of different nickel concentrations as well as nickel braze were available for such mixtures. Although relatively constant nickel and variable molybdenum concentrations could be

obtained, this seems unlikely. The molybdenum found in the spacer wire (see Table VI) is also disturbing. These difficulties are not believed to be related to recent reproducibility problems with the microprobe. Contamination of the specimen surface seems possible.

Analysis of nickel braze is also shown in Table VII and apparently indicates the degree of bonding obtained. Iron and chromium in the braze were found to be in about the same ratio as in the materials joined. Material balance for the analyzed elements of the braze was 96.5%.

The metallic particle within the fuel was a mixture of noble-metal fission products and stainless steel as indicated in Table VII. In addition to fission-product molybdenum and ruthenium, technetium was detected in this particle. Rhodium and palladium were probably also present, but not detected at the low concentrations. A material balance of only 78.6% was obtained. Although counting rates of the fission-product elements were somewhat variable, iron, chromium, and nickel counting rates were found uniform. A spectral scan of the particle did not reveal missing elements, but oxygen and other light elements were not checked. Despite the poor material balance, this particle appears deficient in chromium.

The pellets of this section were fuel of nominal composition. Some small particles of urania were located at the edge of one pellet before the fuel was covered by residual polishing agents exuded from the cracks of the fuel. After repolishing, no urania particles were found.

Figure 84 represents mounted section 118A23L2. The melted steel in this section appeared to be a mixture of Types 304 and 316 stainless steel. Counting rates for molybdenum in the melted steel were variable and indicated approximately the range of concentrations found in section 118A30R2 (see Table VII). Counting rates for molybdenum corresponding to those expected from Type 316 stainless steel were found in the outer band of steel (A, at the top of Fig. 84) and in the remnant fuel cladding. Very low molybdenum concentrations were indicated for Type 304 stainless steel in the next band of steel (B) and in the spacer wires (C). Another narrow band of steel (D) adjacent to and partially melted into the mass of melted steel was structurally the same as the narrow band (10) shown in Fig. 83. The molybdenum counting rate of this band varied along its length, but appeared reasonably uniform across its width. Molybdenum content of this band increased from essentially zero (Type 304 stainless steel), where the band was optically distinct ( $D_1$ ), to about that of the massive melted steel adjacent to the melted region of the band ( $D_2$ ). A decrease of molybdenum contained in the melted steel along the interface from  $E_1$  to  $E_2$  is noted with the progressive dissolution of the Type 304 stainless steel band.

Small metal particles distributed within a fragmented fuel pellet and widely scattered in association with fuel fragments throughout this section



were found to be either stainless steel or stainless steel alloyed with noble-metal fission products. Images at about 340X magnification for metal particles of both types within the fragmented fuel pellet (F) are presented in Fig. 85 (Region F of Fig. 84). Sample current and elemental distributions of iron, chromium, nickel, manganese, molybdenum, ruthenium, uranium, and plutonium are shown. Technetium was also detected, but at too low a concentration for imaging. Noble-metal fission products were incorporated in only two of three particles. Manganese had a tendency to concentrate along the edges of both types of particles.

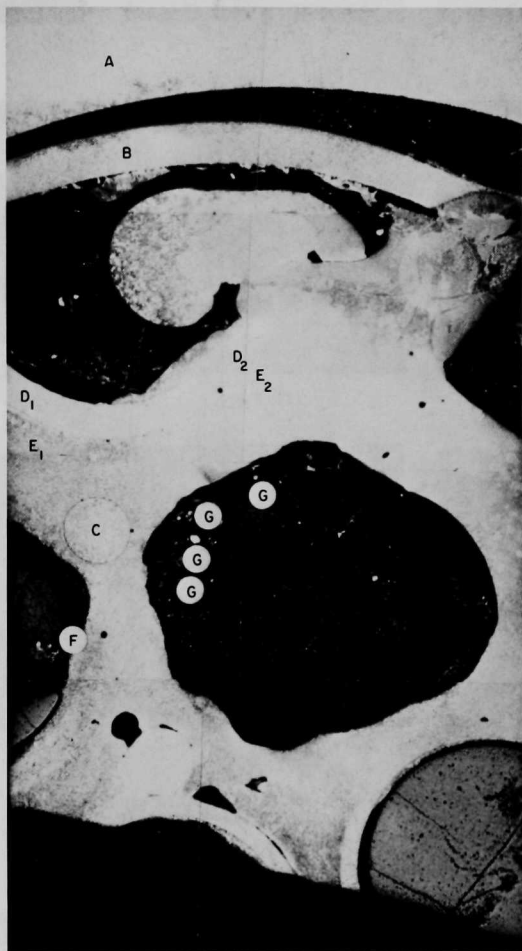


Fig. 84. Section 118A23L2, Showing Locations of Microprobe Analysis. Mag. ~11X. Neg. No. MSD-181996.

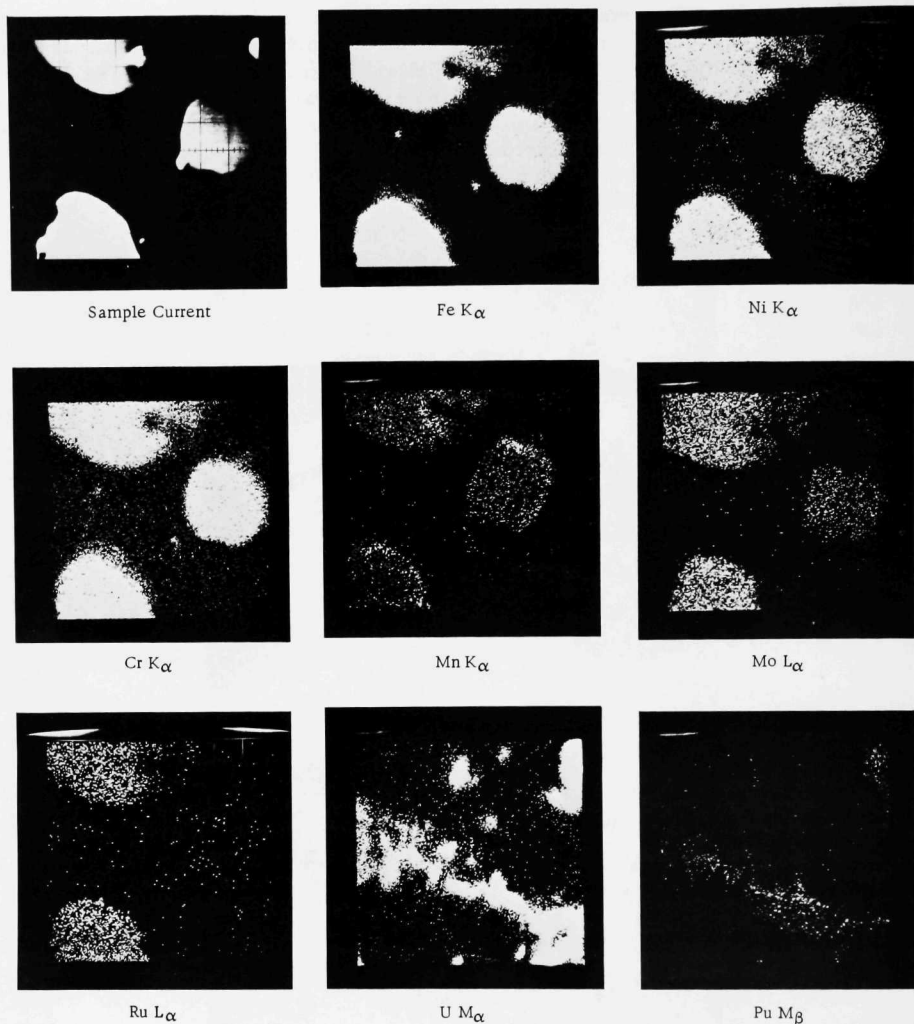


Fig. 85. Sample Current and Elemental Distribution Images of Two Types of Steel Particles from Section 118A23L2. Mag.  $\sim 340\times$ . Neg. Nos. MSD-181991, -181993, -181992, -181994, and -181995.

Counting was performed semiquantitatively for iron, nickel, chromium and molybdenum for four particles not containing noble metals. These particles were within the central hole of massive melted metal (G) shown in

Fig. 84. One particle was essentially Type 316 stainless steel with about 50% chromium depletion. The other particles appeared to be mixtures of Types 316 and 304 stainless steels with up to 20% chromium depletion. The chromium depletion apparently increased as the proportion of Type 316 stainless steel increased.

Small particles of fuel were distributed extensively within this section. Only two pieces of urania were found outside of the partially intact element locations (H). One element location (F) contained a portion of the urania insulator pellet and a large piece of fuel; the other such location (I) contained only urania. Urania locations were outlined in Fig. 84.

## V. DISCUSSION AND ANALYSIS OF TEST L3, RUN 2

A. Scenario Constructed from Examination and Correlation of Experimental Data

The events in Test L3-2 that are of interest are the times and locations for the start of coolant boiling, gas release and voiding, dryout of cladding, melting of cladding, movement of cladding, melting of fuel, and movement of fuel. A reconstructed history of these events constitutes a scenario of the transient. In forming a scenario from the experimental data, we must bear in mind that the available data generally do not provide direct, unequivocal indications of the occurrence or places of these events. An exception is the hodoscope information, which is directly related to fuel movement. For the rest, inferences have to be made, and some of the reasoning involved is outlined in Sec. B below.

Figure 86 presents the scenario for Test L3-2 on a time scale that provides a graphical impression of the intervals between the various events. Only the beginnings of the various processes are shown. All the processes will extend spatially in the test section as time goes on, and it is difficult to determine when they end. Most likely they overlap in time, so that eventually there is simultaneously, and in different locations, boiling, dryout, melting, and motion of molten cladding and fuel. The data cannot resolve the times and locations of all events exactly. However, some feel for the degree to which experimental observations track these events may be obtained from the tabulation of comments that follows the scenario (see Table VIII).

A scenario can also be constructed from the results of calculations with the SAS code. Such a scenario is presented in Sec. C below. These

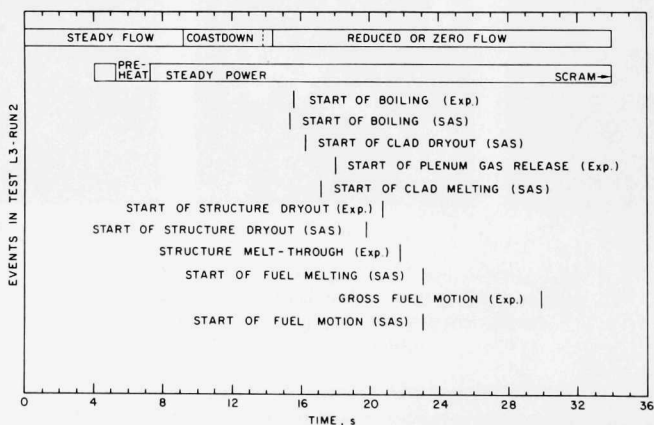


Fig. 86. Scenario from Test L3, Run 2

TABLE VIII. Instrumental Responses to Events in Test L3, Run 2

Start of Boiling	
Time, s	Responses Related to Start of Boiling
15.6	Upper flowmeter shows slight flow increase; lower flowmeter shows slight flow decrease.
~15-16	Lower pressure transducer shows irregularity (pressure increase) relative to previous and subsequent readout.
15.4	TC7 shows inflection in temperature.
15.4	TC10 shows temperature leveling off.
15.5	TC11 shows temperature leveling off.
Gross Boiling, Gas Release, and Voiding	
Time, s	Responses Related to Boiling, Gas Release and Voiding
15.8	Flow rates become equal, cross over, and become erratic with respect to each other.
17.2	Upper flowmeter shows spike in flow rate.
18-19	Upper pressure transducer shows general pressure rise.
17-19	Lower pressure transducer shows general pressure rise.
16.2-17.2	TC4 shows outlet coolant temperature leveling off for a brief maximum, then dropping sharply. Erratic behavior follows.
16.4-17.0	TC5 shows behavior similar to TC4, but the maximum is less pronounced. Erratic behavior follows.
16.4-19	TC7 shows temperature leveling off and then rising gradually.
16.0-19	TC8 shows temperature leveling off and then rising gradually.
15.8-19	TC9 shows temperature leveling off and then rising gradually.
Before 20.6	TC10 and 11 show temperature leveling off and then rising gradually.
~16.6-20.6	TC12 shows generally decreased rate of temperature rise, roughly paralleling TC10 and 11.
21.6 and 21.9	Upper flowmeter shows spike in flow rate that may be due to gas release.
21.7-21.8	Lower flowmeter shows greater negative flow oscillation that may be due to gas release and corresponds to response of upper flowmeter.

TABLE VIII (Contd.)

Dryout	
Time, s	Responses Related to Dryout
19 onward	Upper and lower pressure transducers show continued, but more gradual, pressure rise.
17 onward	Inlet coolant flow rate is oscillatory, with a small amplitude averaging about zero.
~18 onward	Outlet coolant flow rate is erratic, more so than inlet flow rate, and is generally positive with occasional, small negative peaks.
<22.2	TC1 shows rapid temperature rise just before failure, indicating dryout. Cladding and structure melting occurred before this time, probably somewhere along leads.
17-21	TC4 shows temperature erratically constant [oscillating ~50°F]. TC5 readout appears hard to correlate--erratic.
17.5-29.8	TC7, 8, and 9 show closely bunched temperatures at about 1800-1845°F (982-1007°C), generally rising to the latter temperature at 29.8 s, the time of the major incident of the experiment.
16-20.4	TC10 and TC11 show temperature fairly steady before rising rapidly toward structure failure.
17.5-20.5	TC12 shows temperature rising, not quite as level as for TC10 and TC11, before going up rapidly toward structure failure.
Cladding and/or Structure Melting	
Time, s	Responses Related to Melting
20.6	TC10 shows sharp rise in temperature from previous plateau.
21 ± 1	Signal from lower pressure transducer averages to a fairly steady value before showing about a 20% rise during the period 22-25 s. The steady period might correspond to cladding melting, and the subsequent rise might be due to further gas expansion.
~22	Upper pressure transducer shows leveling of pressure.
<22.2	TC1 shows rapid rise in readout and failure--probably due to meltthrough of leads at a point up on the column.
~20	TC7, 8, and 9 show temperature curve flattening out.

TABLE VIII (Contd.)

23.0-24.0	TC10 showed temperature constant [2518°F (1381°C)] for about 1 s. The temperature rose sharply [2534°F (1390°C)] and briefly, and TC10 failed. The last small rise could be due to the junction no longer being just Chromel-Alumel.
22.4	TC11 failed, indicating a temperature of 2516°F (1380°C).
21.8-22.0	TC12 failed between these two times, having been rising steeply just before.
	The above thermocouple failures result directly from structure failure, which implies cladding melting and failure at somewhat earlier times than those indicated.

## Axial Fuel Motion

Time, s	Responses Related to Fuel Motion
29.8-30.5	Hodoscope data show fuel movement. Flowmeters show strong perturbations in flow, including flow reversal (lower flowmeter). Pressure transducers show pressure excursions. TC4, 7, 8, and 9 show a temperature spike at 30.0 s.

calculations can provide a scenario that is rich in details, such as vapor-bubble growth, movement, and collapse; extent of film dryout; temperature distribution in fuel pins; location and extent of cladding melting; and location and extent of fuel melting and motion. As suggestive of our understanding as this detail may be, only part of it can be checked against reality--at least at this time. Figure 86 shows those items that can be compared with the scenario that was derived from the experimental data.

#### B. Rationale behind Scenario Deduction

The start of boiling is expected to be accompanied by flow perturbations. A growing vapor bubble would tend to accelerate the surrounding sodium upward and downward, so that the upper flowmeter would show increased flow and the lower one decreased flow. In principle, since boiling is an endothermic process, there might also be a reduction in rate of temperature rise and, if boiling is extensive enough, leveling off of temperature. Extensive boiling, of course, also could be identified with voiding, and similar temperature behavior might be associated with voiding. Boiling, implying bubble and void formation, would result in some volume increase in the system, displacing sodium upward and causing an observed pressure rise because of the raised head. Bubbling and voiding, to the degree that they are erratic and accompanied by collapsing bubbles and voids, would be expected to send shocks through the sodium and register as irregularities in pressure (which may not be detectable on the high-range pressure transducers).

In principle, voiding could be identified and assessed by comparing inlet and outlet coolant flow rates. The differences between the time integrals of the flow rates would reflect the void volume at various times. However, the small flow rates during the period of interest in Test L3, together with the instrumental and analog-to-digital-conversion uncertainties (discussed above), make an attempt at reliable void calculation not very promising.

Gas release from the pins is a process that can overlap with and be hard to distinguish from the start of boiling and, particularly, voiding. Flow-meter responses are expected to be similar for all three events. If there are fissures in the cladding that could provide early escape paths for the gas before the cladding yields, then the separate identification of gas release and start of boiling become clouded. As a general rule, if gas release could occur only after the cladding is weak enough to rupture because of its elevated temperature (such as after dryout), then start of boiling would be expected to precede gas release.

Dryout can be conceived as occurring at two kinds of surfaces: on the cladding and on the structure. Since the pins are the heat source, cladding will probably dry out at a given axial location before the nearby structure does so. In the dryout region, there must have been prior voiding. Dryout as a process of film evaporation is an endothermic process and would tend to stabilize the local temperature. Vapor generated by dryout of cladding would result in a volume expansion and pressure rise, so that the sequence of cladding dryout to structure dryout might be reflected by the structure thermocouples as two temperature plateaus (or leveling-off regions) with an intervening interval of rising temperature. The temperature difference can be related to a pressure increase that results from (1) the expansion of sodium vapor that has been going on, thereby raising the head of liquid sodium above the voided region, and/or (2) the release of pin gas, which also raises the pressure head. Above a dried-out region, there is likely to be a zone of refluxing sodium. This condition is likely to result in erratic flow rates and pressures. The upper instruments would probably show more scattered response than the lower ones, since the lower ones are buffered by the sodium on the pump side of the loop.

Melting of cladding could be reflected, too, in a tendency for a nearby thermocouple to give a stabilized temperature readout because of the effect of the endothermic nature of melting. Also, pressure might tend to be stabilized because the melting occurs in a voided and dried-out region so that no further vapor would be generated; and since the temperature tends to be stable, there would be little or no thermal expansion of vapor. By this token, a tendency toward equality of inlet and outlet flow rates could be expected.

A delayed indication of cladding melting might be obtained if TC1 should show an otherwise unexplained rapid temperature rise. This rise could conceivably result from rundown of molten cladding into the inlet region



with consequent heating of the sodium surrounding TC1, though this does not seem to have happened in L3. The observed failure of structure thermocouples adjacent to the fuel column, always after a preceding rapid temperature rise, is interpreted as the result of structure meltthrough, either at the location of the thermocouple junction, or higher up next to the thermocouple leads. Of the functioning structure thermocouples, only TC11 and TC12 would have been liable to have their leads destroyed in this way, because only these thermocouples had parts of their leads adjacent to the fuel column. TC10 had its junction next to the top of the fuel column, so that failure of TC10 was likely to occur at the junction. The observed failure of TC1 was probably due to meltthrough of its leads somewhere next to the fuel region, rather than to a catastrophic event at its junction in the sodium.

Cladding movements can be deduced only uncertainly, if at all, from the instrumental data. A "prior-time" deduction can be made from thermocouple failure because some time must have passed before the failure when cladding melted and presumably moved. This assumes that it is unlikely that the forces on a segment of molten cladding are so nicely balanced that the molten cladding remains stationary. Downward flow under gravity is only one possibility. If it occurs, temperature rises might be recorded by lower thermocouples (if any survive). However, upward movement of molten cladding is also possible as a result of vapor and/or gas streaming. A sudden disruptive gas release could even splatter cladding sideways. All these events would influence thermocouples near them.

Fuel melting also can be identified only tentatively from the instrumental readout during the transient. The thermocouples nearest the melting site would probably have failed by the time fuel melts, so that data from only the more distant surviving thermocouples would be available for comment. It is hard to predict whether the general response would be to show only the generally rising temperature of the transient, or whether the rise would be depressed by the endothermic process of melting.

Fuel movement, if it is a slow collapse and if no criticality complications arise, would probably be expected to cause instrument responses similar to those observed for cladding movement. However, if there is a rapid dispersal, a general, erratic response of surviving instruments would be expected. The hodoscope, of course, provides the definitive, direct data on fuel movement.

Clearly, considerable judgment is involved in these interpretations of data from the test-section instruments. Some clarification comes from the hodoscope, neutron radiographs, and posttest dissection of the loop, bearing in mind that the latter two sources deal only with the test section in a frozen state that formed after the transient. The interpretive uncertainty arises in good part because the portions of the sequence are not amenable to clear-cut differentiation. For example, the processes of boiling and voiding overlap,

since voiding is boiling progressing at a rate that is high enough to form a vapor bubble that embraces the cross section of the fluted tube. Furthermore, drying is really the terminal stage of boiling, and it becomes plain that boiling, voiding, and dryout are an integral sequence that is separated into these components only somewhat arbitrarily. Gas release complicates these events even more. Additional complications arise because, realistically, the phenomena have not only an axial dimension, but a radial one as well. For example, at a given axial location, a region around the central pin may be voided, but a region between outer pins may just be boiling. It would be arbitrary to state that, at this axial location under these conditions, only boiling, voiding, or dryout were occurring.

### C. Commentary on the Scenario

#### 1. Comments on Instrumental Data, Excluding Hodoscope

Perhaps the most important point to consider in interpreting the scenario is that the deduced timing reflects time lags in the effect of an event in registering on an instrument, thermocouples particularly. Uncertainties in interpretation can also affect the deduced timing. The start of boiling, for example, is shown in Table VIII as possibly related to various instrument responses in the period 15-16 s. Of these responses, the ones from the flowmeters appear to give the clearest sign of a change at 15.6 s, and if a specific time is to be given for start of boiling, this is probably the best available from experimental data.

The small inflections shown by TC4, TC5, TC8, and TC9 from 12 to 14 s can be regarded as indications of preboiling phenomena. Such events might include pin motion, like bowing (see hodoscope data), as the temperature rises and changes in the flow distribution. This time period comes during the last part of coastdown, and the flow pattern is expected to become less turbulent. The very noticeable leveling of temperature reported by TC12 at 14.2 s most likely reflects a postcoastdown change in flow pattern rather than indicating boiling. Boiling at this time is questionable because the temperature at TC12 was about 320°F (178°C) lower than at TC10 and TC11, and those thermocouples have not yet recorded a boiling-temperature plateau.

In the period from about 16 to 17 s, TC4 and TC5 showed temperatures going through a maximum--particularly so for TC4. Such responses are believed to result from extended boiling. The reason for the difference in behavior between TC4 and TC5 might lie in the geometry of the thermocouple positions: TC4 was located over a central channel, whereas TC5 was located over the edge of the fluted tube. With the erratic up and down movement of sodium that might be expected at this level to attend boiling, the central, more exposed location of TC4 would be expected to lead to more fluctuation in temperature than would the more protected, side-line location of TC5.

Dryout can be considered as occurring on two kinds of surfaces: the cladding and the structure. A further distinction is made between the process of drying out and the state of being dried out, because usage of the term "dryout" can sometimes be ambiguous if the meaning is not clarified. The process of drying out is considered to occur in a coolant-voided region in which the coolant film on a surface (cladding or structure) is evaporating; the final state of the surface is "dried out."

For the interval most likely covering early dryout, about 16-20.5 s, the most reliable indicators are probably TC10, TC11, and TC12 because they are most closely situated to the probable dryout zones. TC10 and TC11, particularly, showed two temperature plateaus in this period that are taken to reflect mainly cladding dryout from about 16 to 17.5 s, and mainly structure dryout from about 19 to 20.5 s.

The temperature difference between the two plateaus is regarded as reflecting an increase in pressure. If the cladding was drying out during the first plateau and started melting (SAS calculations indicate that about 1 s separates the appearance of a dried-out cladding area and the melting of cladding in that area), then gas release from the pin(s) would result in an increase in pressure in the test section. Scoping calculations on the probable effect of releasing the pin-plenum and fission gases indicate pressure rises (about 8 psi) and concomitant rises in the sodium saturation temperature [about 80°F (44°C)] that correspond reasonably well with the observations.

It appears reasonable to expect that, with continued energy input, continued vaporization of sodium will occur and the drying out process will progress. This continued process might be expected to be accompanied by sodium refluxing in the region of TC7, TC8, and TC9 above the fuel column.

The behavior of the inlet flowmeter from 17 to 28.5 s is noteworthy. In this period, the flow was oscillatory, with a frequency of 3.3 Hz from 17 to 22 s, and of 5 Hz from 22 to 28 s. These frequencies are lower than they were for the much-smaller-amplitude oscillations in the start-of-boiling region from 15.5 to 16 s, namely 10 to 7 Hz. If the oscillations reflect vapor-bubble growth and collapse (condensation), then a decrease in frequency might reflect a gas release that would cause a decrease in condensation rate. By this token, gas release could be expected as early as 17 s.

Another feature of the inlet flow oscillations is the nodal nature of the envelope of the oscillations. Partial "nodes" are seen at 17, 20.5, 23.4, 25.2, 26.0, 26.6, 27.5, and 28.5 s. One conjecture is that these correlate with bursts of gas release. Another conjecture is that they correlate with minor motion of the fuel. Indeed, the hodoscope data showed fuel moving in various ways during this time. A detailed account of the fuel motion appears in Sec. IV.C.

Thermocouples on the fluted tube failed in the order TC12, TC11, and TC10. This order is what would be expected if the location of the greatest temperature rise in the fuel pins tended toward the midplane, which was the region closest to TC12. TC1 failed at 22.7 s, shortly after TC11 and TC12 failed (22.4 and 21.8-22.0 s, respectively). This is consistent with the idea that TC1 failed because its leads were melted through somewhere adjacent to the fluted tube. Possibly, this meltthrough occurred at or near the levels of TC11 and TC12. Furthermore, the flow peaks registered by the upper flowmeter at 21.6 and 21.9 s might be related to the thermocouple failures. If the flow peaks correlate with gas releases, then we can speculate that the gas bursts might have driven molten steel to the fluted tube and/or aided in the rupture of the fluted tube at the levels of the thermocouples.

After TC10 failed, the surviving instruments gave no easily interpretable forecast of the eruption at 29.8 s. This ostensibly peaceful period, of course, might not appear so featureless if there were instrumentation to record events such as the lost thermocouples might have. Indeed, the hodoscope revealed considerable activity in the fuel. As it is, we can adduce refluxing, as discussed above in connection with dryout, in the TC7-TC9 region, probably as a variable-thickness film. The refluxing action, while smooth in the film region, might be manifested at a higher location by slugs of sodium rising and reentering. Such behavior can explain the erratic response at this time of TC4 and TC5 in the outlet sodium.

When the eruption did occur, it was relatively mild. Fission-gas pressure, steel vapor pressure, and fuel vapor pressure have been proposed as possible energy sources for the eruption. Of these, sudden fission-gas-pressure release at 29.8 s is the least likely because the gas would probably have been released when cladding failed sometime between cladding dryout and cladding melting, perhaps as early as about 12 s before the eruption. In fact, the responses of TC10, TC11, and TC12 and of the pressure transducers were interpreted, in the dryout discussion above, as consistent with the release of gas from the pins at this time. The exact contributions of fuel and cladding vapor pressures to the total pressure would depend on temperature and hence on location. This matter will now be examined.

Molten Type 316 stainless steel at high temperatures may reasonably be treated as essentially an ideal solution. In this case, the partial vapor pressures of the components are given by  $p_i = p_i^0 x_i$ , where  $p_i^0$  is the vapor pressure of the pure component at the given temperature and  $x_i$  is the atom fraction of the component in the steel. Figure 87 shows the partial pressures of the major components of Type 316 stainless steel (iron, chromium, and nickel) over the molten steel and the total vapor pressure of the steel. In addition, the vapor pressure of  $\text{UO}_2$  is shown.

An exact examination of the system would require that further details of fuel chemistry in the test situation be known, particularly the

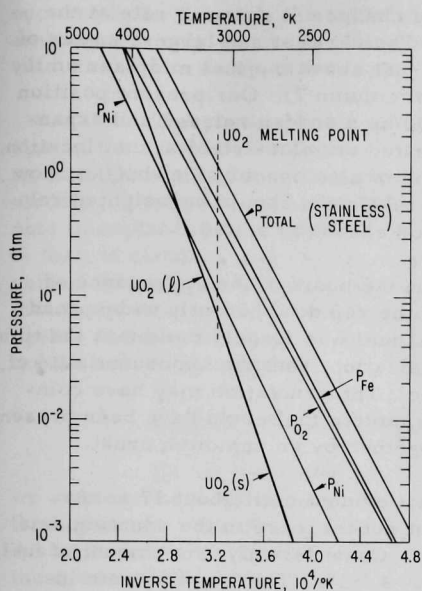


Fig. 87. Vapor Pressures of Fuel and Stainless Steel

implications of the pressure of  $\text{UO}_3$ . For example, at  $2240^\circ\text{K}$ , the dominant vapor species over a mixed-oxide fuel with  $\text{O}/\text{M} = 1.98$  is  $\text{UO}_3$ ; only about one-third of the total fuel vapor pressure comes from  $\text{UO}_2$ . However, neglecting this aspect in the present discussion, we see from Fig. 87 that, below about  $4000^\circ\text{K}$ , the total vapor pressure of the stainless steel components is greater than the vapor pressure of  $\text{UO}_2$ . The steel vapor pressure is 1 atm at about  $3100^\circ\text{K}$ , at which point the  $\text{UO}_2$  vapor pressure is about 0.06 atm. When the  $\text{UO}_2$  vapor pressure is 1 atm (about  $3600^\circ\text{K}$ ), the steel vapor pressure is about 6.6 atm. An immiscible system of stainless steel and fuel at  $3600^\circ\text{K}$  could therefore be expected to exert a total vapor pressure of at least 7.6 atm from just these components, with the steel contributing the most. Other volatile species (such as  $\text{UO}_3$  discussed above) will contribute further increments to the total pressure.

From Fig. 87 it appears that the curve of  $\text{UO}_2$  vapor pressure crosses that of the stainless steel total vapor pressure near  $4000^\circ\text{K}$ . At this temperature, therefore, fuel vapor pressure could start to dominate. In a rising-temperature situation, as in the experiment, if steel and fuel are in close proximity, cladding vapor pressure would be exerting the greater force until about  $4000^\circ\text{K}$  was reached. Close proximity of molten cladding and fuel could result in several ways. One way is for molten fuel to fall on a steel plug. The fuel could be hot enough to vaporize the steel, or continued neutron heating of the fuel would also drive up the temperature. Another route to generation of steel vapor pressure is for globules of molten steel in molten fuel to be focal points for vapor-pressure buildup as temperature rises until the vapor bursts forth. In this connection, superheating of the steel globules and sudden, virtually explosive vaporization could explain delayed release of vapor pressure.

## 2. Comments on Hodoscope Data

The fuel motions revealed by the hodoscope are consistent with the events that were deduced from the other experimental data and that were codified in the scenario. A number of conclusions from the hodoscope data were deduced, in addition to the direct implications that were described earlier in this report. They are presented now.

The timing and direction of the changes in counting rate at the start of the eruption were investigated. The earliest and largest losses of fuel occurred in a region about 4 in. long, just above the fuel midplane on the pump side of the fuel column (Rows 7-10 of column 7). Our present position is to suggest that the eruption was impelled by a sudden release and expansion of stainless steel vapor from superheated stainless steel at that location. A contribution of vapor from the fluted tube is also conceivable, but just how the contributions from cladding and fluted tube steel should be weighted relative to each other in the generation of vapor cannot be stated.

Although we might conclude, on the basis of the appearance of the fuel in the posttest examination and of the rapid, apparently widespread initiation of the eruption, that the central fuel was largely molten at the time of the eruption, there is no unequivocal indication from the hodoscope data of liquid flow (or slumping) prior to this time. The eruption may have coincided with widespread fuel melting. Also, molten fuel could have been present in the interior of pellets that were held together by an unmolten crust.

Axial motion of the fuel was not evident until about 17 s. As Fig. 39 shows, by 17.5 s there was a slight net increase in the counting rate in Row 3 and a net decrease below Row 12. Quantitatively, the amount of fuel below Row 12 seemed to have decreased by  $4 \pm 1\%$ . The counting rate increased in Row 3 of columns 9, 7, and 6 was equivalent to an upward motion of about 0.1 in. This motion was not uniform across the top of the fuel since some of the detectors in Row 3 showed an essentially uniform signal at this time. Subsequently (after 17.5 s), the deficit below Row 12 decreased and then increased again, as shown in Table IX.

TABLE IX. Fuel Deficit below Row 12

Time, s	Deficit, %	Time, s	Deficit, %
17.5	$4.0 \pm 1.0$	23.5	$9.3 \pm 1.0$
19.0	$0.7 \pm 1.0$	26.0	$9.7 \pm 1.0$
20.5	$2.3 \pm 1.0$	29.3	$3.0 \pm 1.0$
22.0	$5.0 \pm 1.0$		

A hypothesis to explain this decline in counting rate and its accompanying upward motion of fuel is that fission gases that probably were being released or had been released by this time (about 18 s) exerted an upward force on the higher fuel pellets in a given pin, and moved them up slightly against the restraining force of the spring above the spacer tube. Variations between pins can explain the nonuniform upward motion. If an open channel remained in some pins for pressure of released fission gas to equalize with the pressure of pin-plenum gas, no net force for pellet displacement would have remained; or, if pellets in some pins were jammed inside the cladding tightly enough to resist any upward force from fission gas, no movement would have



occurred. In Test L4, the initial decline in overall counting rate below Row 12 amounted to only about 1%. Since the L4 fuel had a fully developed central void, there was an opportunity to vent the fission gases into the plenum.

The postulate that fission gases contributed to the initial expansion of the L3 fuel is supported. On the matter of gas release, it is pertinent to note that the SAS calculations, as indicated in the scenario, suggest that cladding dryout and melting started at about this time. A further point to note in explaining why pellets in some pins may not have moved at this time is that, if cladding melted, as suggested by SAS, fission gas could have been vented through the breached cladding before displacing pellets. Note, too, that the posttest examination also showed pin-dependent compression of the spring and displacement of the spacer tube. Pin-dependent displacement of the fuel, then, is credible.

### 3. Interpretation and Correlation of Results of Posttest Examination

To set the context of the discussion of posttest examination results, we summarize the hodoscope results. Major axial fuel motion, as revealed by the hodoscope, occurred about 16 s after the end of coolant flow coastdown. A single eruption, centered about 1 in. above the original fuel midplane, voided much of the midregion of the fuel column. The displaced fuel moved mostly upward, slightly downward, and somewhat laterally. There was no evidence of earlier slumping or of subsequent reentry. By about 8 s before the eruption, fuel was moving (perhaps "rattling about" is an apt expression) as pellets or as fragments of pellets rather than as coherent pins. Penetrations of the fluted tube occurred between this time and the major movement.

From the posttest examination, heat generation seemed to have been greatest near the midlength of the original fuel column and on the side away from the pump. The consistency of this with the hodoscope data was discussed in Sec. IV.D.4. The cladding and spacer wires apparently melted first, but not uniformly on all pins. As the melted steel flowed downward and approached heat sinks--such as insulator pellets, bottom end plugs, and structural components like the header--it cooled off. Sufficient heat was apparently contained within the molten steel to allow some of it to dribble down among the end plugs, ending up on the side of the cluster toward the pump. Some small dribblets found their way to the bottom bend of the loop.

As heating continued, the gas from the pins was probably released as the temperature of the fluted tube approached its melting point. The effect of gases released from the pins could not be deduced from the posttest results. Presumably, the pressure of fission gases would result in fuel swelling, chiefly in the radial direction. The frozen fuel had a different distribution of gases from that in Test L2, as was evident from spherical voids within grains (not observed for Test L2) and irregular voids among the grains. In general, the voids in Test L3 seemed to be smaller than for Test L2, except in a few

instances where frothlike particles were observed. However, the total voidage for both Tests L3 and L2 was similar.

As stated, the hodoscope indicated that fuel motions of various sorts occurred before the major axial movement. Perhaps slumping was prevented by swelling of the solid fuel by the expanded, hot fission gases. The mass of the swollen fuel column may have been partially supported by the surrounding structure. Molten steel in contact with the hot fuel would probably find its way into the pores in the fuel. As the temperature rose, the vapor pressures of the steel components would tend to rise. However, superheating of steel globules is possible, so that the equilibrium vapor pressures corresponding to a given temperature would not be generated until the limit of superheat was reached. Then, sudden release of the vapor would ensue. Since the fission gases and the pin-plenum fill gas do not go through a change of state, pressure buildup from these gases would keep pace with their temperature rather than be manifested as a sudden burst. The formation of the few frothlike particles of fuel that were found was more likely to have involved fission-gas expansion than vaporization of a liquid.

The stainless steel among the bottom end plugs, with its contained fuel particles, probably achieved its position as a result of the eruption, and in that sense constituted a second flow of steel. The flow reversal at the bottom agrees with this supposition. Compared to Test L2, neither fuel nor steel in Test L3 accumulated to the same extent at the bottom of the pins as a result of melting.

At the upper end of the fuel column, the energy of eruption was expended in lifting and pushing molten fuel against unmolten fuel pellets, thereby forcing the hot, unmolten fuel and insulator pellets up into the spacer tubes. In two pins, the hot fuel melted through the cladding above the top of the original fuel column. Energy was consumed in crushing the pellets into the spacer tubes, lifting the spacers, and compressing the springs. The motion imparted to the spacer tubes compressed the nonuniformly heated springs beyond their yield strength on the bottom end. After the eruption, three of the spacers remained up against the springs, but the other four dropped down. Even though the yield strength of the spring material was exceeded, the yield strength of the similar cladding material adjacent to the spring was not exceeded, since there was no increase in cladding diameter. Surface-tension effects of melted steel would contribute to the distribution of steel around the upper blockage.

The fuel-column region below the upper blockage was filled with sodium, but the space around the plenums of the pins was not. Since the level of sodium in the pump side of the loop appeared to be close to that of the top of the fuel pins, the sodium around the plenums must have flowed through channels in the blocked region down into the fuel region. No indication was found of movement of sodium through the bottom blockage during cooling.



#### 4. SAS2B Calculations

A scenario for Test L3 was constructed from the output of calculations using the SAS2B code.\* This scenario is presented in Table X.

TABLE X. Scenario Derived from SAS Calculations

Time, s	Event and Comments
15.41	Boiling starts.
16.30	Coolant void extends from 7.9 in. above the bottom of the fuel column to 3.6 in. above the top of the fuel; 42% of the length of the fuel column region is voided. Cladding is dry over 33% of the fuel column, from 8.5 in. above the bottom to 0.5 in. below the top of the fuel column.
17.01	First cladding melting occurs at a point 0.7 in. above the fuel midplane.
17.25	Cladding is dry over 67% of the length of the fuel column, from 4 in. above the bottom of the fuel to 0.5 in. below the top. Cladding is molten in part of this range.
19.02	Cladding is molten and moving over 34% of the fuel column length, in the region between 5 in. above the bottom and 3.9 in. below the top of the fuel column.
19.82	Cladding blockage forms 1.8 in. above the top of fuel column. Structure dries out 0.67 in. above the fuel midplane.
20.72	Partial cladding blockages occur 0.9 and 2.6 in. above the bottom of the fuel region.
22.52	First fuel melting becomes noticeable with a melt fraction of 0.003-0.005 over a range of about 1.1 in. just above the fuel midplane.
23.09	First indication of slumping appears.
23.51	Slumping has occurred over a 2.25-in. range (17% of fuel-column length), the lower part of which is at the fuel midplane. Structure is dry down to 0.6 in. above the bottom of the fuel column and up to 1.6 in. below the top of the column.
24.51	Fuel slumped over 43% of its length, from 1.6 in. below the fuel midplane to 4.2 in. above.

A comparison of the timing of major events as abstracted from the SAS output with the corresponding timing as deduced from experimental data (see Fig. 86) shows generally good agreement. One point of difference, though, is that the present version of SAS when used with the SLUMPY code predicts slumping, whereas no slumping was revealed by the hodoscope. Further refinement of the code to handle slumping is indicated.

\*M. G. Stevenson, W. R. Bohl, F. E. Funn, T. J. Heames, G. Hoppner, and L. L. Smith, "Current Status and Experimental Basis of the SAS LMFBR Accident Analysis Code," Proc. Fast Reactor Safety Meeting, CONF-740401, Beverly Hills, Calif., p. 1303 (Apr 2-4, 1974).

## APPENDIX

Test-section Characteristics

The thermohydraulic and structural characteristics of the test section are important in determining the test conditions and results. Several axial fuel-pin and test cross-section parameters are given in Table A.1. The detailed test cross section is shown in Fig. A.1.

TABLE A.1. Axial Parameters of Fuel Pin and Cross Section of Test L3

Total pin length	20.875 in.
Fuel length	13.5 in.
Insulator pellets	
Top	0.5 in.
Bottom	0.5 in.
Axial reflector (Inconel)	
Top	6.0 in.
Bottom	a
Plenum volume	0.15 in. <sup>3</sup>
Flow area per pin	0.0062 in. <sup>2</sup>
Hydraulic diameter	0.120 in.
<u>Heated perimeter<sup>b</sup></u>	
Wetted perimeter	0.539
<u>Cladding and space-wire area</u>	
Flow area	0.314
<u>Fuel area</u>	
Flow area	0.783
<u>Steel area<sup>c</sup></u>	
Cladding and space-wire area	2.24
<u>Total area<sup>d</sup></u>	
Flow area	2.4

<sup>a</sup>A 3.4-in.-long solid steel lower end fitting was below the insulator pellets in the test pins.

<sup>b</sup>Cladding perimeter, does not include spacer wire.

<sup>c</sup>Includes fluted tube.

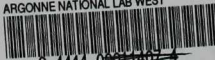
<sup>d</sup>Total area in the flow area plus the area between the fluted tube and the outer wall of the adiabatic holder.



## ACKNOWLEDGMENTS

We acknowledge the substantial contributions from a number of people who were involved in the preparation, performance, and analysis of Test L3. Particularly, we appreciate the helpful discussions with J. G. Eberhart, the computer graphics from P. H. Froehle, and the early design and planning from J. P. Tylka, R. T. Purviance, and R. G. Palm. In addition, we recognize the contributions of the staff and technicians of the Fuel Dynamics Operations Group, and of J. F. Boland, L. J. Harrison, and the TREAT Operations Group. Administrative facilitation of the work came from R. O. Ivins and C. E. Dickerman.

ARGONNE NATIONAL LAB WEST



3 4444 00011007 4